

# 12

## Fast nuclear rotation – the cranking model

At very high spin, one expects the Coriolis and centrifugal forces to disturb strongly the wave functions of many nucleons. As discussed in the introduction to the previous chapter, it then becomes desirable to treat all nucleons on the same footing.

In this chapter, we will introduce two models of this kind, namely the cranking model and the rotating liquid-drop model. The cranking model is first applied to the simple harmonic oscillator potential to illustrate some different concepts. Then the Nilsson–Strutinsky cranking approach corresponding to a combination of the two models is introduced. Within this approach, phenomena like band terminations and superdeformed high-spin states are discussed.

### 12.1 The cranking model

In the cranking model, the rotation is treated in the classical sense with the rotation vector coinciding with one of the main axes of the nucleus. It then turns out that, in this system, the nucleons can be described as independent particles moving in a rotating potential. In fact, the rotation degree of freedom enters in very much the same way as the deformation degrees of freedom, which were introduced in chapters 8 and 9. One important shortcoming of the cranking model is that the wave functions are not eigenstates of the angular momentum operator. Instead, the angular momentum is generally identified with the expectation value of its projection on the rotation axis.

The mathematical formulation of a rotating single-particle potential was first given by Inglis (1954). With the coordinates in the laboratory system given by  $x, y$  and  $z$  and those in the rotating system by  $x_1, x_2$  and  $x_3$ , we get,

for constant angular velocity,  $\omega$ , around the  $x_1$ -axis

$$\begin{aligned}x_1 &= x \\x_2 &= y \cos \omega t + z \sin \omega t \\x_3 &= -y \sin \omega t + z \cos \omega t\end{aligned}$$

Apart from some phase-factor, the time-dependent wave functions in the two systems must satisfy

$$\psi^\omega(x_1, x_2, x_3, t) = \psi(x, y, z, t)$$

which leads to

$$\left(\frac{\partial \psi}{\partial t}\right)_{x,y,z} = \left(\frac{\partial \psi^\omega}{\partial t}\right)_{x_1,x_2,x_3} + \frac{\partial \psi^\omega}{\partial x_2} \frac{\partial x_2}{\partial t} + \frac{\partial \psi^\omega}{\partial x_3} \frac{\partial x_3}{\partial t}$$

With

$$\begin{aligned}\frac{\partial x_2}{\partial t} &= \omega(-y \sin \omega t + z \cos \omega t) = \omega x_3 \\ \frac{\partial x_3}{\partial t} &= \omega(-y \cos \omega t - z \sin \omega t) = -\omega x_2\end{aligned}$$

we now find

$$\frac{\partial \psi(x, y, z, t)}{\partial t} = \left(\frac{\partial}{\partial t} - i\omega \ell_1\right) \psi^\omega(x_1, x_2, x_3, t)$$

where the angular momentum operator  $\ell_1$  is given by

$$\ell_1 = -i \left( x_2 \frac{\partial}{\partial x_3} - x_3 \frac{\partial}{\partial x_2} \right) = -i \left( y \frac{\partial}{\partial z} - z \frac{\partial}{\partial y} \right) = \ell_x$$

The equality between  $\ell_1$  and  $\ell_x$  is easily proven by direct evaluation.

The relation for the time derivatives implies that the time-dependent Schrödinger equation for  $\psi$

$$i\hbar \frac{\partial \psi(x, y, z, t)}{\partial t} = h\psi(x, y, z, t)$$

is transformed into

$$i\hbar \frac{\partial \psi^\omega}{\partial t}(x_1, x_2, x_3, t) = (h - \hbar\omega \ell_1) \psi^\omega(x_1, x_2, x_3, t)$$

for the wave function in the intrinsic system,  $\psi^\omega$ . In these equations, the Hamiltonian is given by  $h$  to point out that it is a one-particle operator. This is in contrast to the total Hamiltonian, which is denoted by  $H$  (in the preceding chapters, no such distinction has been made and a capital  $H$  has been used also for the single-particle Hamiltonian).

The Schrödinger equation in the rotating system can now be solved in the standard way as an eigenvalue problem

$$(h - \hbar\omega j_1) \phi^\omega = e^\omega \phi^\omega$$

where the orbital angular momentum operator  $\ell_1$  has been generalised to cover also particles having an intrinsic spin and has thus been replaced by  $j_1$  ( $\mathbf{j} = \ell + \mathbf{s}$ ). The Hamiltonian in the rotating system,

$$h^\omega = h - \hbar\omega j_1$$

is also referred to as the cranking one-particle Hamiltonian. The eigenvalues  $e_i^\omega$  are referred to as the single-particle energies in the rotating system or more properly Routhians. This is so because the Hamiltonian in the rotating system does not overlap with the energy. The cranking one-particle Hamiltonian may be summed over all the independent particles of the system to obtain the total cranking Hamiltonian,

$$H^\omega = H - \hbar\omega I_1$$

Alternatively, the cranking Hamiltonian can be derived by direct use of the rotation operator  $\mathcal{R} = \exp(-il_x\omega t)$  (see e.g. de Voigt, Dudek and Szymanski, 1983) or from the Lagrangian (problem 12.1).

A simple way to obtain the cranking Hamiltonian is to minimise the energy

$$E = \langle \Psi | H | \Psi \rangle$$

under the constraint that the total spin

$$I = \langle \Psi | I_1 | \Psi \rangle$$

is fixed. The rotational frequency  $\omega$  (or rather  $\hbar\omega$ ) will then take the role of a Lagrangian multiplier, which, as seen from the derivation above, can be identified with the rotational frequency.

The energies of the particles are measured in the laboratory system and are calculated as

$$e_i = \langle \phi_i^\omega | h | \phi_i^\omega \rangle$$

where it should be observed that the time-independent wave functions,  $\phi_i^\omega$ , are not eigenvectors of the Hamiltonian,  $h$ . Similarly, the angular momentum is calculated as an expectation value

$$\langle j_x \rangle_i = \langle \phi_i^\omega | j_x | \phi_i^\omega \rangle = \langle \phi_i^\omega | j_1 | \phi_i^\omega \rangle$$

The total energy and the total spin are now given as sums over the occupied orbitals:

$$E_{\text{sp}} = \sum_{\text{occ}} e_i$$

$$I \approx I_x = \sum_{\text{occ}} \langle j_x \rangle_i$$

In a similar way as for deformed nuclei at spin zero (chapter 9), these summed quantities can on average be renormalised to liquid-drop behaviour. We will, however, first study the pure harmonic oscillator potential within the cranking model. For this potential, no renormalisation is necessary.

## 12.2 The rotating harmonic oscillator

Many of the effects observed or expected at high spin can be illustrated in the rotating harmonic oscillator potential. It is then very advantageous that the single-particle wave functions and corresponding energies are given by closed expressions (Valatin, 1956). In the present discussion of the harmonic oscillator, we mainly follow Cerkaski and Szymański (1979). We will thus introduce some approximations so that the minimal energy and corresponding shape for different spins  $I$  can also be determined analytically. With these approximations, the details of the solutions should not be given too much significance but the main trends are illustrated very nicely.

In the pure oscillator, the intrinsic spin is uncoupled from the spatial coordinates. We thus only consider the orbital angular momentum, which gives the cranking Hamiltonian

$$h^\omega = h_{\text{osc}} - \omega \ell_1$$

where

$$h_{\text{osc}} = -\frac{\hbar^2}{2m} \Delta + \frac{1}{2} m (\omega_1^2 x_1^2 + \omega_2^2 x_2^2 + \omega_3^2 x_3^2)$$

and

$$\ell_1 = (x_2 p_3 - x_3 p_2)$$

Boson creation and annihilation operators are now introduced in a similar way as in chapter 8:

$$x_i = -i \left( \frac{\hbar}{2m\omega_i} \right)^{1/2} (a_i^+ - a_i), \quad p_i = \left( \frac{\hbar m \omega_i}{2} \right)^{1/2} (a_i^+ + a_i)$$

for  $i = 1, 3$  and

$$x_2 = \left( \frac{\hbar}{2m\omega_2} \right)^{1/2} (a_2^+ + a_2), \quad p_2 = i \left( \frac{\hbar m \omega_2}{2} \right)^{1/2} (a_2^+ - a_2)$$

With the special phases chosen (Bohr and Mottelson, 1975), one finds that, for example, the matrix elements of  $\ell_1$  are real. The Hamiltonian  $h^\omega$  is obtained as

$$h^\omega = \sum_{i=1}^3 \hbar \omega_i \left( a_i^+ a_i + \frac{1}{2} \right) - \omega \ell_1$$

where

$$\ell_1 = \frac{\omega_2 + \omega_3}{2(\omega_2 \omega_3)^{1/2}} (a_2^+ a_3 + a_3^+ a_2) - \frac{\omega_2 - \omega_3}{2(\omega_2 \omega_3)^{1/2}} (a_2^+ a_3^+ + a_2 a_3)$$

It is possible to make a transformation among the operators  $a_2^+, a_2, a_3^+$  and  $a_3$  (i.e. among the coordinates  $x_2, x_3$  and the momenta  $p_2, p_3$ ) to bring the Hamiltonian into the form of three uncoupled harmonic oscillators, but as mentioned above, here we will introduce some approximations to make the solution more transparent.

While the first term of the  $\ell_1$  operator couples orbitals within the same major oscillator shell, the second term couples orbitals of  $(N, N \pm 2)$  shells (where, as usual, the  $N$ -shells are defined in the stretched basis,  $N \equiv N_t$ ). For small and intermediate deformations, the energy spacing between such orbitals belonging to different  $N$ -shells is large. Furthermore, the coefficients of the two terms differ by a factor  $(\omega_2 - \omega_3)/(\omega_2 + \omega_3)$ , which is far below unity for reasonably small deformations. We thus conclude that the  $\Delta N = 2$  couplings of the  $\ell_1$  operator are generally much less important than the  $\Delta N = 0$  couplings. Consequently, we neglect the second term of the  $\ell_1$  operator.

The remaining part of  $h^\omega$  is now diagonalised by a unitary transformation

$$a_2^+ = a_\alpha^+ \cos \phi + a_\beta^+ \sin \phi, \quad a_3^+ = -a_\alpha^+ \sin \phi + a_\beta^+ \cos \phi$$

which leads to

$$\begin{aligned} h^\omega &= \hbar \omega_1 \left( a_1^+ a_1 + \frac{1}{2} \right) + \frac{\hbar \omega_2}{2} + \frac{\hbar \omega_3}{2} \\ &\quad + \hbar a_\alpha^+ a_\alpha \left( \omega_2 \cos^2 \phi + \omega_3 \sin^2 \phi + \omega \frac{\omega_2 + \omega_3}{(\omega_2 \omega_3)^{1/2}} \cos \phi \sin \phi \right) \\ &\quad + \hbar a_\beta^+ a_\beta \left( \omega_2 \sin^2 \phi + \omega_3 \cos^2 \phi - \omega \frac{\omega_2 + \omega_3}{(\omega_2 \omega_3)^{1/2}} \cos \phi \sin \phi \right) \end{aligned}$$

$$+\hbar(a_\alpha^+a_\beta + a_\beta^+a_\alpha) \left( (\omega_2 - \omega_3)\cos\phi\sin\phi - \omega \frac{\omega_2 + \omega_3}{2(\omega_2\omega_3)^{1/2}} (\cos^2\phi - \sin^2\phi) \right)$$

To get  $h^\omega$  in the form of three uncoupled oscillators, we must require the mixed operators to disappear

$$(\omega_2 - \omega_3)\cos\phi\sin\phi - \omega \frac{\omega_2 + \omega_3}{2(\omega_2\omega_3)^{1/2}} (\cos^2\phi - \sin^2\phi) = 0$$

The angle  $\phi$  is thus obtained as

$$p = \tan 2\phi = \frac{\omega}{\omega_2 - \omega_3} \frac{(\omega_2 + \omega_3)}{(\omega_2\omega_3)^{1/2}}$$

where the notation  $p$  ( $= \tan 2\phi$ ) has been introduced as a measure of the rotational frequency,  $\omega$ . We now get the Hamiltonian  $h^\omega$  in the following form

$$h^\omega = \hbar\omega_1 \left( a_1^+ a_1 + \frac{1}{2} \right) + \hbar\omega_\alpha \left( a_\alpha^+ a_\alpha + \frac{1}{2} \right) + \hbar\omega_\beta \left( a_\beta^+ a_\beta + \frac{1}{2} \right)$$

with the frequencies of the normal modes given by

$$\omega_{\alpha,\beta} = \frac{1}{2}(\omega_2 + \omega_3) \pm \frac{1}{2}(\omega_2 - \omega_3)(1 + p^2)^{1/2}$$

The single-particle eigenvalues of  $h^\omega$  are

$$e_v^\omega = \hbar\omega_1 \left( n_1 + \frac{1}{2} \right) + \hbar\omega_\alpha \left( n_\alpha + \frac{1}{2} \right) + \hbar\omega_\beta \left( n_\beta + \frac{1}{2} \right)$$

where  $n_1, n_\alpha$  and  $n_\beta$  specify the number of quanta in the three normal-mode degrees of freedom.

A further quantity of interest is the expectation value of  $\ell_1$ . The diagonal parts of this operator are easily obtained and thus, for an orbital characterised by the occupation numbers  $n_1, n_\alpha$  and  $n_\beta$

$$\langle \ell_1 \rangle = \langle n_1 n_\alpha n_\beta | \frac{p}{(1 + p^2)^{1/2}} (a_\beta^+ a_\beta - a_\alpha^+ a_\alpha) | n_1 n_\alpha n_\beta \rangle = \frac{p}{(1 + p^2)^{1/2}} (n_\beta - n_\alpha)$$

We will now consider total quantities of the  $A$ -particle system with the  $A$  particles filling the orbitals (generally those being lowest in energy) of the rotating harmonic oscillator. For this purpose we define the quantities

$$\Sigma_k = \sum_{v \text{ occ}} \langle v | a_k^+ a_k + \frac{1}{2} | v \rangle = \sum_{v \text{ occ}} \left( n_k + \frac{1}{2} \right)_v$$

The index  $k$  takes the values  $k = 1, \alpha$  and  $\beta$  (or  $k = 1, 2$  and  $3$  for  $\omega = 0$ )

and the summation runs over the occupied orbitals,  $|v\rangle$ . The total energy in the rotating system is given by

$$E^\omega = \sum_{\substack{v \\ \text{occ}}} \langle v | h^\omega | v \rangle = \hbar\omega_1\Sigma_1 + \hbar\omega_\alpha\Sigma_\alpha + \hbar\omega_\beta\Sigma_\beta$$

In the cranking model, the angular momentum is identified with the sum of the expectation values of  $\ell_1$

$$I = \sum_{\substack{v \\ \text{occ}}} \langle v | \ell_1 | v \rangle = \frac{p}{(1+p^2)^{1/2}} (\Sigma_\beta - \Sigma_\alpha)$$

Thus, each configuration is associated with a maximum angular momentum,  $I_{\max}$ , with

$$I_{\max} = \Sigma_\beta - \Sigma_\alpha$$

The energy that will result from a measurement (in the laboratory system) is calculated as the sum of the expectation values of the static Hamiltonian  $h_{\text{osc}}$ :

$$E = \sum_{\substack{v \\ \text{occ}}} \langle v | h_{\text{osc}} | v \rangle = \sum_v \langle v | h^\omega + \omega\ell_1 | v \rangle = E^\omega + \hbar\omega I$$

For a fixed configuration, i.e. fixed values of  $\Sigma_1, \Sigma_\alpha$  and  $\Sigma_\beta$ , and for a fixed spin  $I$ , we now want to find the potential shape that minimises the energy  $E$ . For this purpose, the energy is rewritten in the form

$$E = \hbar\omega_1\Sigma_1 + \hbar\omega_2\tilde{\Sigma}_2 + \hbar\omega_3\tilde{\Sigma}_3$$

where

$$\tilde{\Sigma}_{2,3} = \frac{1}{2} (\Sigma_\alpha + \Sigma_\beta) \mp \frac{1}{2} (I_{\max}^2 - I^2)^{1/2}$$

This simple formula for the energy  $E$  is obtained only if a further approximation is made, namely

$$p = \frac{\omega_2 + \omega_3}{\omega_2 - \omega_3} \frac{\omega}{(\omega_2\omega_3)^{1/2}} \approx \frac{2\omega}{\omega_2 - \omega_3}$$

In the derivation, it is also useful to note that  $p = I/(I_{\max}^2 - I^2)^{1/2}$  or  $(1+p^2)^{1/2} = I_{\max}/(I_{\max}^2 - I^2)^{1/2}$ .

For fixed values of  $\Sigma_1, \tilde{\Sigma}_2$  and  $\tilde{\Sigma}_3$ , it is straightforward to find the minimum under the volume conservation constraint (cf. chapter 8):

$$\omega_1\omega_2\omega_3 = \omega_0^3$$

The following relation results:

$$\omega_1 \Sigma_1 = \omega_2 \tilde{\Sigma}_2 = \omega_3 \tilde{\Sigma}_3$$

The frequencies  $\omega_1, \omega_2$  and  $\omega_3$  are obtained as

$$\omega_i = \omega_0^0 \left( \Sigma_1 \tilde{\Sigma}_2 \tilde{\Sigma}_3 \right)^{1/3} / \tilde{\Sigma}_i$$

(with  $\tilde{\Sigma}_1 \equiv \Sigma_1$ ). These values of the frequencies correspond to a shape adjusted to minimise the energy  $E$  for any value of the spin  $I$  ( $I \leq I_{\max}$ ) and for any configuration specified by  $\Sigma_1, \Sigma_\alpha$  and  $\Sigma_\beta$  (or by  $\Sigma_1, \Sigma_2$  and  $\Sigma_3$  in the limit of  $I = 0$ ). The minimised energy  $E$  can be written in the concise form

$$E = 3\hbar \omega_0^0 \left( \Sigma_1 \tilde{\Sigma}_2 \tilde{\Sigma}_3 \right)^{1/3} = 3\hbar \omega_0^0 \left[ \Sigma_1 \left( \Sigma_\alpha \Sigma_\beta + \frac{1}{4} I^2 \right) \right]^{1/3}$$

For  $I = I_{\max}$ , i.e. for maximal spin within a configuration, we note that  $\tilde{\Sigma}_2 = \tilde{\Sigma}_3$ . Thus, the formula for the frequencies shows that  $\omega_2 = \omega_3$ , which corresponds to a potential being axially symmetric around the rotation axis. For such a shape, the rotation is not collective but instead built from individual nucleons having their spin vectors quantised along the rotation axis, so-called rotation around the symmetry axis.

If the formula for the frequencies is combined with the definitions of  $\varepsilon$  and  $\gamma$  (chapter 8), it is possible to calculate  $\varepsilon$  and  $\gamma$  as functions of spin  $I$  (see problem 12.3)

$$\varepsilon = \frac{3 \left( \Sigma_1^{-2} + \tilde{\Sigma}_2^{-2} + \tilde{\Sigma}_3^{-2} - \Sigma_1^{-1} \tilde{\Sigma}_2^{-1} - \tilde{\Sigma}_2^{-1} \tilde{\Sigma}_3^{-1} - \tilde{\Sigma}_3^{-1} \Sigma_1^{-1} \right)^{1/2}}{\Sigma_1^{-1} + \tilde{\Sigma}_2^{-1} + \tilde{\Sigma}_3^{-1}}$$

$$\tan \gamma = \frac{\sqrt{3} \left( \Sigma_1^{-1} - \tilde{\Sigma}_2^{-1} \right)}{\Sigma_1^{-1} + \tilde{\Sigma}_2^{-1} - 2\tilde{\Sigma}_3^{-1}}$$

We will finally consider the moment of inertia in the simple harmonic oscillator model. For collective rotation with a constant moment of inertia,  $\mathcal{J}$ , the energy is given by  $E = (\hbar^2/2\mathcal{J})I^2$  (in the case of rotation around one axis, one should use  $I^2$  rather than  $I(I+1)$ , which latter is the proper quantity for three-dimensional quantum-mechanical rotation). For a general function,  $E = E(I)$ , it seems natural to define moments of inertia from the derivatives (Bohr and Mottelson, 1981),

$$\frac{\hbar^2}{\mathcal{J}^{(1)}} = 2 \frac{dE}{dI^2} = \frac{1}{I} \frac{dE}{dI} \approx \frac{E(I+1) - E(I-1)}{2I}$$

and

$$\frac{\hbar^2}{\mathcal{J}^{(2)}} = \frac{d^2 E}{dI^2} \approx \frac{E(I+2) - 2E(I) + E(I-2)}{4}$$

where we also indicate how to define these moments of inertia from measured transition energies,  $E_\gamma = E(I+1) - E(I-1)$ . Note that  $\mathcal{J}^{(1)} = \mathcal{J}^{(2)} = \mathcal{J}$  when  $E = (\hbar^2/2\mathcal{J})I^2$ . The  $\mathcal{J}^{(1)}$  moment of inertia is a direct measure of the transition energies while  $\mathcal{J}^{(2)}$  is obtained from differences in transition energies. Except that  $I(I+1)$  has been replaced by  $I^2$  and the discrete differences are now centred around  $I$ ,  $\mathcal{J}^{(1)}$  is identical to the moment of inertia introduced in chapter 11 and shown in fig. 11.13.

For the harmonic oscillator in the present approximation, it is straightforward to calculate

$$\mathcal{J}^{(1)} = \frac{2(\Sigma_\alpha \Sigma_\beta + I^2/4)^{2/3}}{\Sigma^{1/3}} \frac{\hbar}{\omega_0}$$

$$\mathcal{J}^{(2)} = \mathcal{J}^{(1)} \frac{\Sigma_\alpha \Sigma_\beta + I^2/4}{\Sigma_\alpha \Sigma_\beta - I^2/12}$$

These values might be compared with the static rigid body moment of inertia

$$\mathcal{J}_{\text{rig}} = M \sum_{\text{occ}} \langle v | y^2 + z^2 | v \rangle$$

If we follow the equilibrium shapes of the harmonic oscillator, we obtain (see problem 12.4)

$$\mathcal{J}_{\text{rig}} = \frac{\Sigma_\alpha^2 + \Sigma_\beta^2 - I^2/2}{[\Sigma_1 (\Sigma_\alpha \Sigma_\beta + I^2/4)]^{1/3}} \frac{\hbar}{\omega_0}$$

It turns out that both  $\mathcal{J}^{(1)}$  and  $\mathcal{J}^{(2)}$  are generally below  $\mathcal{J}_{\text{rig}}$ ; at large deformations and small spins even considerably below. One could also note, however, that, for  $I = I_{\max}$ ,  $\mathcal{J}^{(1)} = \mathcal{J}_{\text{rig}}$ .

The solution of the harmonic oscillator presented here is useful because it illustrates general features like shape changes and band terminations. On the other hand, the numerical values of moments of inertia or deformations are somewhat crude. Indeed, as mentioned above, it is possible to solve the full cranking single-particle Hamiltonian for the harmonic oscillator potential. With the resulting single-particle energies as input, it is then possible to calculate the total energy using the same procedure as above, i.e. the volume conservation condition is applied to find the deformations,  $\varepsilon$  and  $\gamma$ , which for each spin  $I$  minimise the total energy,  $E$ . In this case, however, no

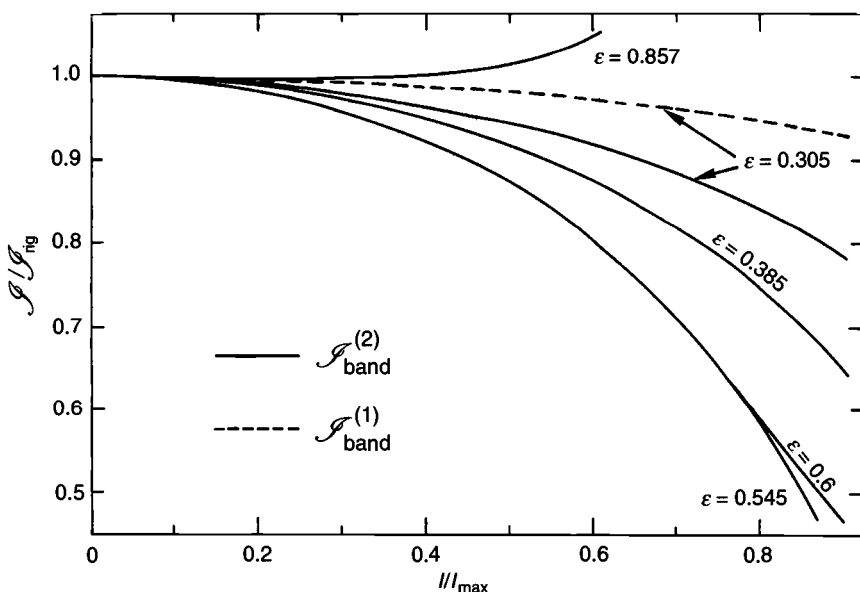


Fig. 12.1. The variation with spin of the moments of inertia  $\mathcal{J}^{(1)}$  and  $\mathcal{J}^{(2)}$  as obtained from the full solution of the cranked harmonic oscillator. The configurations, are labelled by their equilibrium deformations at spin zero, which are all axially symmetric. The moments of inertia and the spin are given in units of the rigid body moment of inertia at the spin zero deformation,  $\mathcal{J}_{\text{rig}}$ , and the maximum spin within the configuration,  $I_{\max}$  (from I. Ragnarsson, 1987, *Phys. Lett.* **199B**, 317).

analytic expressions have been given for  $E(I)$  but a numerical solution is straightforward. One difference (Troudet and Arvieu, 1979) compared with the approximate solution is that only those configurations that are not too deformed ( $\Sigma_3/\Sigma_2 < 1.78$ ) for  $I = 0$  really terminate, i.e. whose rotation becomes non-collective for  $I = I_{\max}$ . The more deformed configurations do not terminate but, instead, they become more and more elongated for very high spins. With the exception of very deformed configurations, both the moments of inertia,  $\mathcal{J}^{(1)}$  and  $\mathcal{J}^{(2)}$ , which start out equal to  $\mathcal{J}_{\text{rig}}$  for  $I = 0$ , decrease with increasing spin, see fig. 12.1. In this figure, the different configurations, which are all axially symmetric for  $I = 0$  ( $\Sigma_x = \Sigma_y$ ), are labelled by their deformation  $\epsilon$  at  $I = 0$ . The spin is given in units of  $I_{\max}$  defined by  $\Sigma_\beta - \Sigma_\alpha = \Sigma_3 - \Sigma_2$  independently of whether any real termination occurs or not, while the unit for the moments of inertia is  $\mathcal{J}_{\text{rig}}(I = 0)$ . With these units, the same figure can be applied to different mass regions. Note, however, that  $I_{\max}$  is strongly dependent on deformation, e.g.  $I_{\max}$  is much larger for an ' $\epsilon = 0.6$  configuration' than for an ' $\epsilon = 0.2$  configuration'.

In the more realistic calculations considered below, we will find that, for strongly deformed configurations in heavy nuclei (superdeformation), the spin will always be much smaller than  $I_{\max}$ . Therefore, we might expect that  $\mathcal{J}^{(2)}$  (as well as  $\mathcal{J}^{(1)}$ ) stays close to  $\mathcal{J}_{\text{rig}}$  for all spins of physical interest. On the other hand, configurations having a smaller deformation at  $I = 0$  might very well reach  $I_{\max}$  at observable spins (band termination). Then, however, the special shell structure caused by the grouping in the  $j$ -shells at  $\varepsilon = 0$  might strongly influence the energies and the pure oscillator can only be used to indicate the general trends.

Besides publications quoted previously in this section, one could mention the papers by Zelevinskii (1975) and by Glas, Mosel and Zint (1978), where additional aspects of the rotating harmonic oscillator are considered.

### 12.3 The rotating liquid-drop model

We will now for a moment ignore the quantal effects and consider the rotation of a nucleus according to the laws of classical mechanics. In such a macroscopic model, the energy is given by

$$E_{\text{macro}}(E, N, \text{def}, I) = E(Z, N, \text{def}) + \frac{\hbar^2 I^2}{2\mathcal{J}(Z, N, \text{def})}$$

The energy  $E(Z, N, \text{def})$  is taken as the static liquid-drop energy, which was treated in chapter 4. The variable ‘def’ denotes a number of deformation parameters, e.g.  $\varepsilon, \gamma, \varepsilon_4, \dots$ . For stable nuclei the liquid drop energy has a minimum for spherical shape. This minimum is caused by the surface energy, which overcomes the deforming tendencies of the Coulomb energy.

In our discussion of the harmonic oscillator, we found that the dynamical moment of inertia was essentially equal to the rigid body value. In the case of independent nucleon motion, this is what is generally expected also for potentials other than the harmonic oscillator. The fact that the experimentally observed moment of inertia is smaller than  $\mathcal{J}_{\text{rig}}$  for low  $I$  can be traced back to the pairing correlations. At higher spins, however, these correlations should disappear. As the rotating liquid-drop model is relevant only at relatively high spins, we will use the rigid body moment of inertia in connection with this model.

The rotational energy becomes smaller with increasing  $\mathcal{J}$ . Thus, with the rigid body value, configurations with the nucleons far away from the rotation axis are favoured. This means that the rotational energy tries to deform the nucleus and this tendency will become dominating for a large enough value of the angular momentum  $I$ .

For small values of  $I$ , the nucleus will behave in a similar way to the rotating earth and become flattened at the poles, i.e. oblate shape with rotation around the symmetry axis. With the rotation axis being the 1-axis and with the definitions of  $\epsilon$  and  $\gamma$  given in chapter 8, this corresponds to  $\gamma = 60^\circ$  (there exists some confusion about the definition of the sign of the angle  $\gamma$  and consequently, oblate shape with rotation around the symmetry axis is sometimes referred to as  $\gamma = -60^\circ$ ). With increasing spin, the distortion of the nucleus will become larger and  $\epsilon$  will increase (still at  $\gamma = 60^\circ$ ). The macroscopic energy of the nucleus  $^{154}\text{Sm}$ , rotating with a spin of  $I = 40$ , is shown as a function of deformation in fig. 12.2.

Detailed calculations, as have been carried out by Cohen, Plasil and Swiatecki (1974), then show that, at sufficiently large angular momentum, the stability towards axial asymmetry is lost. For higher spins, most nuclei will for some intermediate spin values have a minimum for triaxial shape ( $60^\circ < \gamma < 0^\circ$ ) before, for even higher spins, the stability in the fission direction is lost. Thus, the nucleus divides into two fragments, which fly apart due to the centrifugal forces. The  $I$ -values where the transition to triaxial shape and where fission instability sets in, respectively, are shown in fig. 12.3. This figure also shows that, for heavy nuclei, these two  $I$ -values coincide. This means that as soon as the oblate regime becomes unstable the nucleus goes to fission.

## 12.4 An illustrative example of microscopic calculations of high spin states – $^{20}\text{Ne}$

In the discussion of the modified oscillator potential (chapter 6), it was found that no  $\ell^2$ -term was necessary for the light nuclei. This means that, apart from the  $\ell \cdot s$ -coupling term, the single-particle potential of such nuclei is essentially a pure harmonic oscillator. Consequently, the harmonic oscillator has been used quite a lot for the description of light nuclei, especially the sd-shell nuclei. These are the nuclei with the valence protons and valence neutrons in the  $d_{5/2}$ ,  $s_{1/2}$  and  $d_{3/2}$  shells (fig. 12.4), i.e. those having neutron and proton numbers in the range  $N, Z = 8\text{--}20$ .†

The rotating harmonic oscillator should thus be a very useful starting point for the study of high spin states in  $^{20}\text{Ne}$ , which nucleus we will now discuss in some detail. Let us first point out that, for such a light nucleus,  $I = 4$  or  $I = 6$  are already very high spin states, i.e. they correspond to

† In the study of sd-shell nuclei, the symmetry group of the deformed harmonic oscillator, SU(3), has often been used for classification of different configurations. This same symmetry group has also played an important role in elementary particle physics, e.g. for the understanding of the protons and the neutrons as being built out of three quarks.

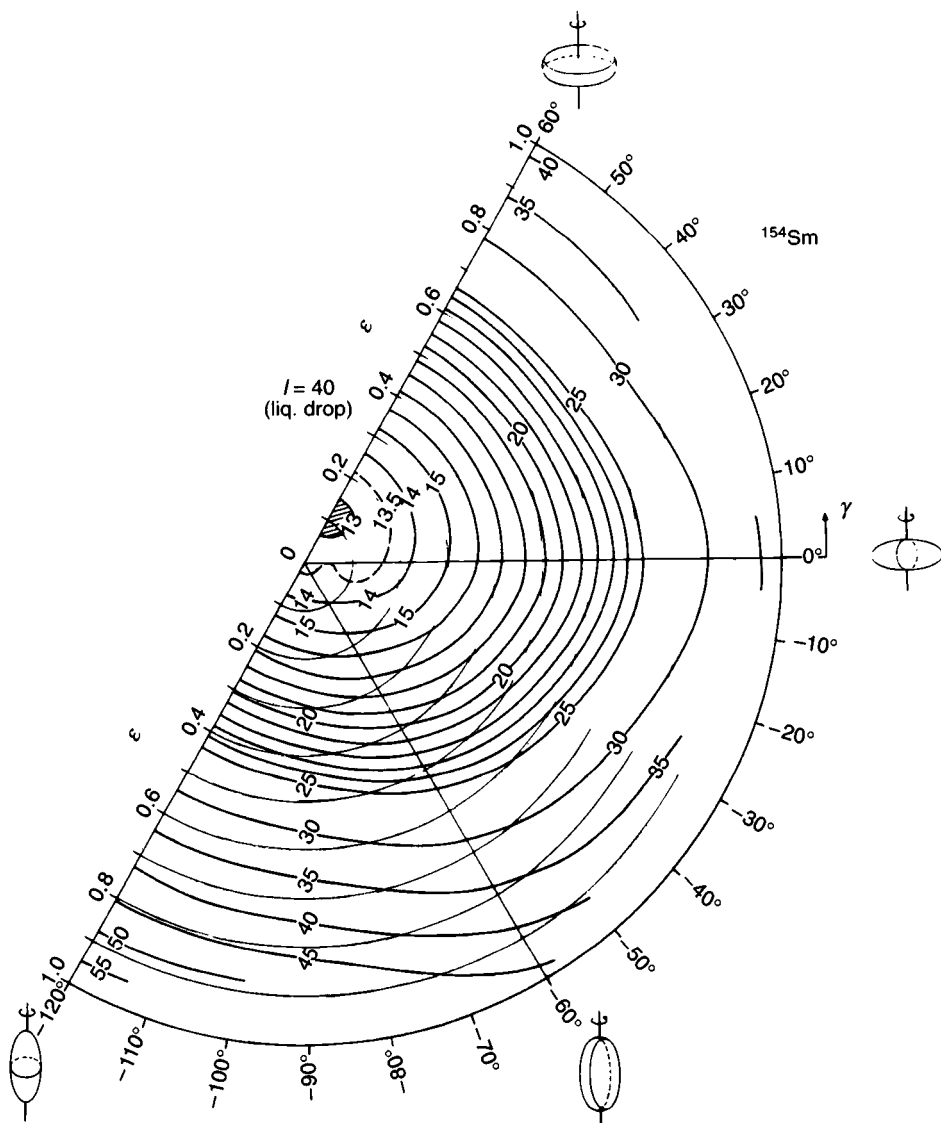


Fig. 12.2. Contour plot in the  $(\epsilon, \gamma)$ -plane of the rotating liquid-drop energy calculated for the nucleus  $^{154}\text{Sm}$  at  $I = 40$ . The rotation axis (defined as the 1-axis) is sketched for the different cases of axially symmetric shape (cf. fig. 8.6). The same nuclear shapes are formed in the three  $60^\circ$  sectors but the rotation axis coincides with the smaller ( $\gamma = 0^\circ$  to  $60^\circ$ ), the intermediate ( $\gamma = 0^\circ$  to  $-60^\circ$ ) and the larger ( $\gamma = -60^\circ$  to  $-120^\circ$ ) principal axis, respectively. The numbers on the contour lines refer to MeV above the energy of a spherical liquid drop at  $I = 0$  (from Andersson *et al.* 1976).



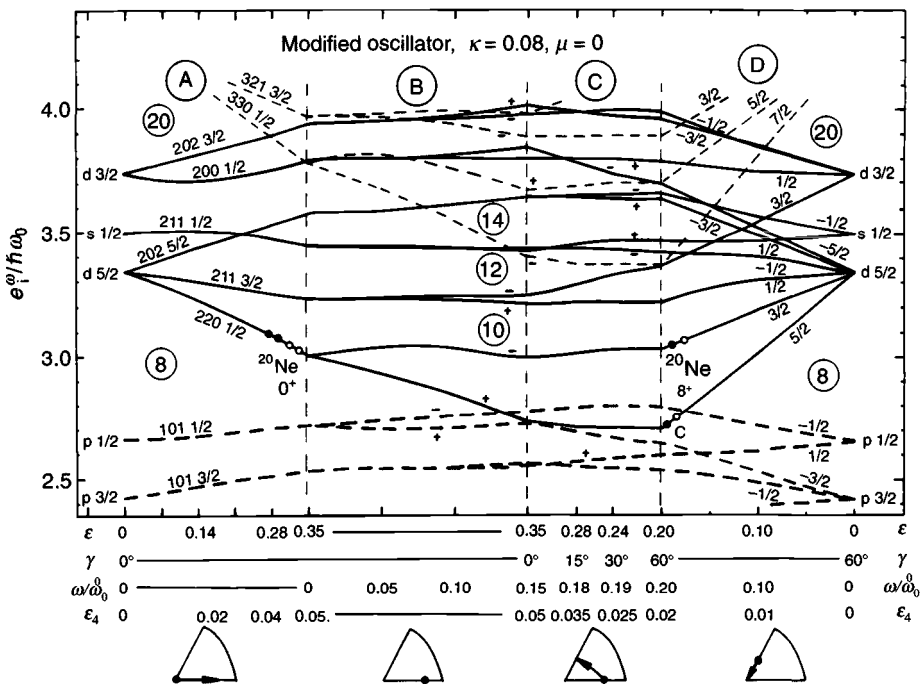


Fig. 12.4. Single-particle orbitals along a path in the  $(\epsilon, \epsilon_4, \gamma, \omega)$  space as indicated schematically in the lower part of the figure. The path is chosen to illustrate how the orbitals can be followed when a prolate collective band goes to termination at oblate shape. The spherical origin of the orbitals at a typical low-spin deformation is traced in part A while in part B, rotation is switched on at constant deformation.

At a frequency of  $\omega/\omega_0 \approx 0.15$  corresponding to  $I \approx 6$  in the  $^{20}\text{Ne}$  ground band, the driving forces toward oblate shape become important. Thus, in part C the deformation is varied over the  $\gamma$  plane together with changes in the other parameters as they occur when a band approaches termination at  $\gamma = 60^\circ$ . In part D, finally, the origin of the aligned oblate orbitals is traced, illustrating to which  $j$  shell they mainly belong and their aligned spin. The occupation of sd-shell orbitals in the ground state and in the terminating  $8^+$  state of  $^{20}\text{Ne}$  is also indicated. It is interesting to note how the  $Z = N = 10$  gap stays large all the way to the termination ( $\epsilon \approx 0.20, \gamma = 60^\circ$ ) while this is not the case for the  $N = Z = 12$  gap. Thus, we expect the aligned  $8^+$  state terminating the ground band in  $^{20}\text{Ne}$  to be more favoured than the corresponding aligned  $12^+$  state in  $^{24}\text{Mg}$  (revised from Sheline *et al.*, 1988).

rotating harmonic oscillator. The present configuration of  $^{20}\text{Ne}$  should thus be denoted as  $\Sigma_\alpha = 14, \Sigma_\beta = 22$  (and  $\Sigma_1 = 14$ ).

In the harmonic oscillator approximation, it is now trivial to calculate the properties of the ground state configuration of  $^{20}\text{Ne}$  from the explicit formulae given above. The maximum spin of the configuration is  $I_{\max} = 8$

( $I_{\max} = \Sigma_\beta - \Sigma_\alpha$ ), a value that can also be deduced from more simple reasoning. With the  $N = 1$  shell being completely filled, the particles in this shell do not contribute to the spin. Thus, eight protons and eight neutrons form an inert core. For particles in the  $N = 2$  shell, the maximum  $\ell$ -value is 2. The double degeneracy in each orbital makes it possible for the two protons and two neutrons to couple independently to  $I = 4$ . The four particles can thus give a total spin of  $I = 8$ . If the intrinsic spin of the particles is also considered, we get the situation illustrated in the upper right part of fig. 12.5. The two protons (or two neutrons) in the  $N = 2$  orbitals (essentially  $d_{5/2}$  orbitals) must have anti-aligned intrinsic spin vectors due to the Pauli principle. Thus, in this case also, the maximum spin is 8. The particles then have their spin vectors quantised along the rotation axis, which means that the nuclear state is axially symmetric around this axis. Furthermore, the four particles rotate mainly around the equator of the nucleus, giving rise to an oblate nuclear shape (fig. 12.5). This was also formally found for the pure oscillator. With the coupling between the different  $N$ -shells being neglected, the nuclear shape is always symmetric at the termination of a band.

The evolution of the proton or neutron single-particle orbitals for the ground band of  $^{20}\text{Ne}$  is illustrated in fig. 12.4. To the far left in this figure, the splitting (and mixing) of the spherical subshells caused by prolate deformation is illustrated. At  $\epsilon \approx 0.35$ , this leads to the orbitals appropriate for the ground state of  $^{20}\text{Ne}$  where two protons and two neutrons fill the [220 1/2] orbital. The potential is now cranked around a perpendicular axis (the  $x$ -axis) leading to a splitting of the doubly degenerate orbitals and new eigenvalues  $e_i^\omega(\omega)$ . Without going into details, we should mention that apart from parity, one more symmetry (associated with rotation, 180°, around the cranking axis) survives so that the orbitals labelled by + and – (signature  $\alpha = +1/2$  and  $\alpha = -1/2$ ), respectively in fig. 12.4 remain uncoupled.

For cranking at a fixed deformation, the slope of the orbitals corresponds to the alignment,  $\langle j_x \rangle = m$ . This is seen from the relation

$$\langle j_x \rangle = -\frac{\partial e_i^\omega}{\partial \omega}$$

which is easily obtained from the cranking Hamiltonian. For prolate shape and small  $\omega$ -values, the two branches of an  $\Omega = 1/2$  orbital get an alignment of  $\pm(1/2)a$  where  $a$  is the decoupling factor discussed in chapter 11 while in lowest order of  $\omega$ , the  $\Omega > 1/2$  orbitals show no alignment (no decoupling factor). Then with increasing rotational frequency  $\omega$ , the coupling between the different orbitals means that all orbitals get a  $\langle j_x \rangle$  different from zero. Note especially that the two orbitals emerging from [220 1/2] become

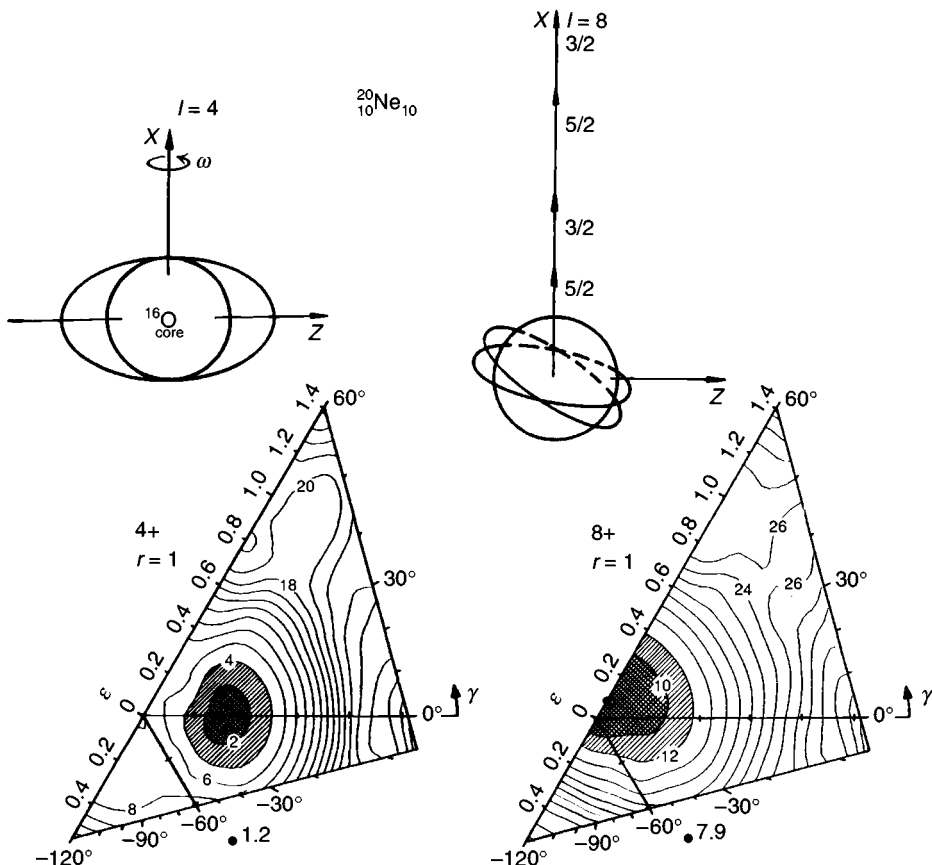


Fig. 12.5. Calculated  $I^\pi = 4^+$  and  $8^+$  energy surfaces with inclusion of the shell energy for  $^{20}\text{Ne}$  together with schematic illustrations of the configurations at the minima. The definition of  $\varepsilon$  and  $\gamma$  is the same as in fig. 12.2. The contour line separation is 2 MeV and the numbers on the lines refer to excitation energy above the spherical liquid drop at  $I = 0$  (from Ragnarsson *et al.*, 1981).

strongly aligned at large  $\omega$ . These are the orbitals occupied in the ground band of  $^{20}\text{Ne}$  as discussed qualitatively above. Their strong alignment corresponds to a polarisation toward oblate shape. Thus, in the third section of fig. 12.4, the shape is followed through the  $\gamma$ -plane with slightly increasing rotational frequency ending up in an oblate nucleus ‘rotating around its symmetry axis’.

The so-called rotation around the symmetry axis deserves some comments. Indeed, from the quantum mechanical point of view, no such rotation is possible as two states rotated by an angle  $\varphi$  relative to each other cannot be distinguished. Even so, the concept is useful when selecting

favoured configurations of single-particle character. Indeed, rotation around a symmetry axis only corresponds to particle–hole excitations for a symmetric nucleus. One problem is then to select those excitations giving favoured energies for different spins (the yrast states). One convenient way to do this is from a diagram as illustrated on the left in fig. 12.6, where the single-particle energies  $e_i$  are plotted versus  $m = \Omega, \Omega$  being the eigenvalue of  $j_x$ . The total spin is simply given by

$$I = \sum (m_i^{\text{part}} - m_i^{\text{hole}})$$

and the excitation energy by

$$E^{\text{exc}} = \sum (e_i^{\text{part}} - e_i^{\text{hole}})$$

where the sum runs over the particle–hole excitations. It is now easy to conclude that the most favoured states are selected from filling the orbitals below the straight line ‘tilted Fermi surfaces’ illustrated in the figure. In this way, states having lowest energy per spin unit will be selected, however only for some spin values. Intermediate spins will then be obtained from particle–hole excitations relative to the tilted Fermi surface.

It is straightforward to conclude that the same results are obtained from the cranking formalism. For ‘rotation around a symmetry axis’,  $j_x = \Omega$  is a good quantum number and the eigenvalues of the cranking Hamiltonian are simply

$$e_i^\omega = e_i - \omega \Omega_i$$

corresponding to straight lines when drawn as functions of  $\omega$ , see right panel of fig. 12.6. Then, if for different frequencies the lowest  $e_i^\omega$  are selected, this is exactly analogous to choosing the points below the straight line Fermi surface (where  $\omega$  corresponds to the slope of the line). This result is important because it now becomes possible to treat all kind of rotations, collective and particle–hole excitations, within the same formalism obtaining the yrast states from filling the lowest eigenvalues  $e_i^\omega$  of the cranking Hamiltonian. Indeed, this is what we already used in our discussion of the harmonic oscillator. Note also that the slope of the tilted Fermi surface is proportional to  $\omega$ , which in this case is only an auxiliary parameter. However, in analogy with the case of collective rotation, it appears natural to refer to it as rotational frequency.

Let us now go back to fig. 12.4 where the part to the right is analogous to the single-particle diagram in fig. 12.6. However, the deformation and the rotational frequency are varied simultaneously so that the spherical subshells are regained to the left in fig. 12.4. It is interesting to note that, by choosing

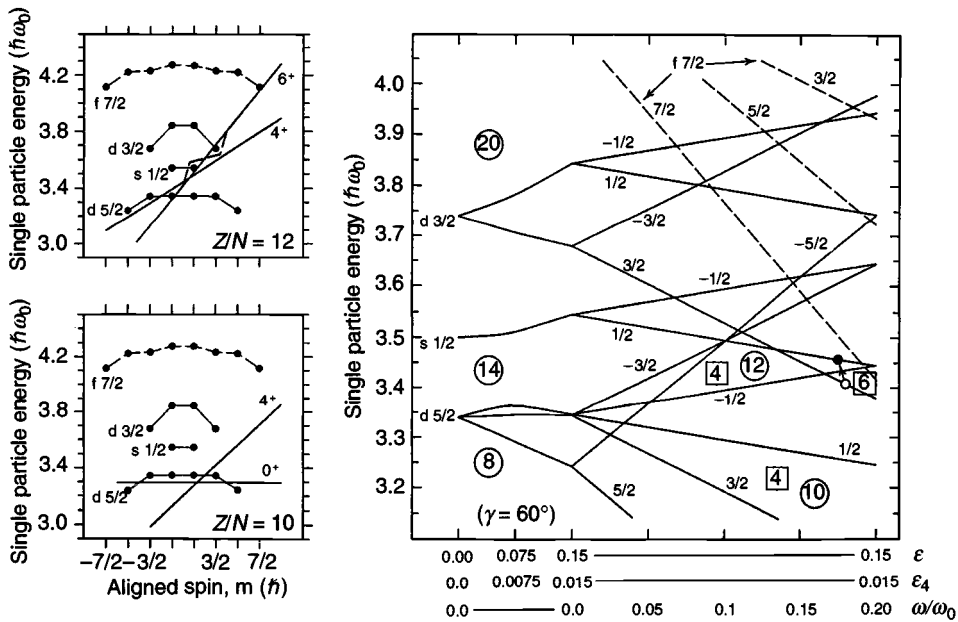


Fig. 12.6. In the left panels, the calculated single-particle energies in the sd-shell region are drawn versus their spin projection on the symmetry axis,  $m_i$ . The deformation is oblate at  $\epsilon = 0.15$ . Sloping Fermi surfaces are then drawn to indicate how different spin states for particle numbers 10 and 12, respectively might be formed at this specific deformation. Whether these configurations are really formed in the spectra of  $^{20}\text{Ne}$  and  $^{24}\text{Mg}$  depends on whether they show up as minima in the energy surfaces or not, i.e. whether that specific deformation is favoured or not at the resulting spin value. The same information can be extracted from the diagram to the right where the spherical origins of the orbitals are first drawn and the ‘rotating energies’,  $e_i - \omega m_i$ , are then followed as functions of  $\omega$ . The numbers enclosed in squares indicate total neutron or proton spin. Note that gaps develop for the same particle numbers and spins where straight line Fermi surfaces could be drawn in the  $e_i$  versus  $m_i$  diagrams. In both approaches is also illustrated (by a long-dashed line and by an arrow, respectively) how an  $I = 5$  state for 12 particles might be formed as a particle–hole excitation from the  $I = 6$  state. Note the large gap that develops to the far right for particle number 10 and the corresponding appearance of the  $e_i$  versus  $m_i$  diagram where there is lots of space for the  $I = 4$  straight line Fermi surface. For particle number 12 on the other hand, no large gap develops and it becomes much more difficult to find space to draw straight line Fermi surfaces in the  $e_i$  versus  $m_i$  diagram.

the path in deformation/rotational frequency illustrated in fig. 12.4, it is possible to follow in a continuous way (no crossings between orbitals) the evolution of  $^{20}\text{Ne}$  from its ground state to the aligned  $8^+$  state.

Using the methods discussed in the next subsection, it is possible to

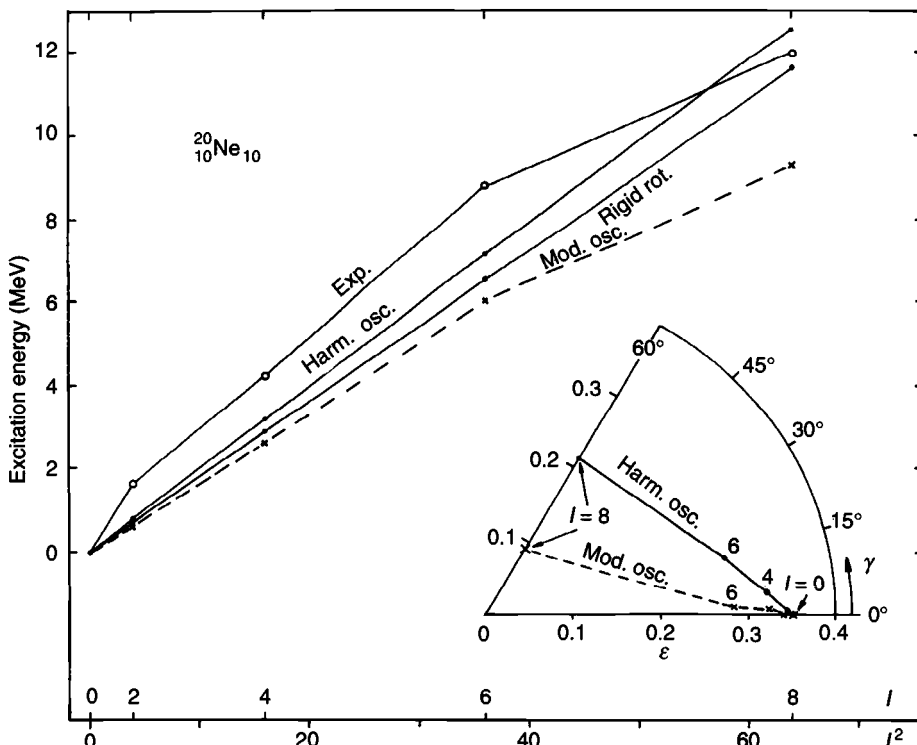


Fig. 12.7. Measured ground band energies of  $^{20}\text{Ne}$  plotted versus  $I^2$  compared with calculated energies in some different approximations. The curve marked ‘Harm. osc.’ shows the energies in the simplified solution of cranked harmonic oscillator while ‘Mod. osc.’ indicates the modified oscillator (fig. 12.5) model. For each spin, the energy is minimised as a function of deformation. The corresponding shapes are shown in the  $(\epsilon, \gamma)$ -plane in the inset. The curve marked ‘Rigid rot.’ gives the energy  $E = (\hbar^2/2J_{\text{rig}})I^2$  where  $J_{\text{rig}}$  is kept constant, equal to the rigid body value at the ground state shape of the harmonic oscillator.

calculate potential energy surfaces also for  $I \neq 0$ . An example of such a calculation is given in fig. 12.5, where the  $I = 4$  and  $I = 8$  energy surfaces of  $^{20}\text{Ne}$  are drawn. The ground state  $I = 0$  shape of  $^{20}\text{Ne}$  is calculated at  $\epsilon \approx 0.35$ ,  $\gamma = 0$ . At  $I = 4$ , the disturbance caused by the rotation is rather small with an essentially unchanged deformation at the potential energy minimum. For  $I = 8$ , the rotational disturbances are much larger and, as anticipated above, the minimal energy shape is oblate with rotation around the symmetry axis ( $\gamma = 60^\circ$ ).

In fig. 12.7, the experimental yrast states are compared with the calculated energies within the harmonic oscillator and modified oscillator models.

Furthermore, we show the energy

$$E = \frac{\hbar^2}{2\mathcal{J}_{\text{rig}}} I^2$$

where  $\mathcal{J}_{\text{rig}}$  is taken as a constant, namely the rigid moment of inertia of the harmonic oscillator at the  $I = 0$  deformation (see problem 12.4). Except for the  $2^+$  energy, the calculated yrast line of the modified oscillator potential (Ragnarsson *et al.*, 1981) is in quite good agreement with experiment. It is especially satisfying that the relatively low energy of the  $I = 8$  state is reproduced. This is in contrast to the harmonic oscillator calculations, which give a much too large  $E_{8+}$  to  $E_{6+}$  spacing. The equilibrium shapes in the two models are also shown in fig. 12.7. The main feature is that the shape remains essentially prolate up to the  $I = 6$  state and that a large change in deformation occurs between  $I = 6$  and  $I = 8$ .

If one goes to higher spins than  $I = 8$  for  $^{20}\text{Ne}$ , one expects an increase of the deformation. In the macroscopic description, this is understood as a result of the centrifugal forces. In the microscopic harmonic oscillator model, particles must be excited to higher shells to get spins above  $I = 8$ . This naturally leads to larger deformations.

The case of  $^{20}\text{Ne}$  is particularly simple because of the axial symmetry ( $\Sigma_1 = \Sigma_2$ ). For a triaxial configuration, there is the possibility to rotate around each of the three principal axis. Three different bands are thus formed but the stability and physical significance of the higher ones is unclear.

The ground state of  $^{24}\text{Mg}$  with  $\Sigma_1 = 16$ ,  $\Sigma_2 = 20$  and  $\Sigma_3 = 28$  is an example of a configuration that is triaxial in the harmonic oscillator approximation (problem 12.5). In the modified oscillator, however, the ground state comes out as essentially prolate (being soft towards  $\gamma$ -deformations) (Ragnarsson *et al.*, 1981; Sheline *et al.*, 1988). The shape evolution with increasing spin is then essentially the same as in the ground band of  $^{20}\text{Ne}$ . Thus, figs. 12.4 and 12.6 can also be used for a qualitative understanding of  $^{24}\text{Mg}$ . Note, however, the high level density at the terminating  $12^+$  state, indicating a competition between different configurations. This is in contrast to  $^{20}\text{Ne}$  where the terminating  $8^+$  state is calculated to be energetically very favoured compared with other states of similar spin.

## 12.5 The shell correction method for $I \neq 0$

When the ground state potential energy has been calculated at some fixed deformation it should be possible to get the  $I$ -dependence simply by adding

the rotational energy as extracted from the cranking model. Thus, for a prescribed spin  $I_0$ , the frequency  $\omega_0$  is determined so that

$$I_0 = \sum_{\substack{i \\ \text{occ}}} \langle j_x \rangle_i$$

Then the excitation energy is obtained as

$$E_{\text{exc}} = \sum_{\substack{i \\ \text{occ}}} e_i|_{\omega=\omega_0} - \sum_{\substack{i \\ \text{occ}}} e_i|_{\omega=0}$$

For example, in fig. 12.5, the Strutinsky shell correction method has been applied to calculate the  $I = 0$  energy surface while the  $I$ -dependence at a fixed deformation has been calculated according to the above formulae. In practice, in each mesh point in deformation space, the cranking Hamiltonian is diagonalised for a number of  $\omega$ -values. Subsequently,  $\omega_0$  and then  $E_{\text{exc}}$  are obtained from interpolation. In the energy surface of fig. 12.5, the energy has also been minimised with respect to  $\varepsilon_4$  deformations.

Very often, however, simple summation to obtain  $E_{\text{exc}}$  might lead to undesired features. In general, this is caused by deficiencies in the single-particle potential so that the average behaviour of  $E_{\text{exc}}$  is unrealistic. For example, the (unphysical)  $\ell^2$ -term in the modified oscillator potential corresponds to a velocity-dependence and leads to an average moment of inertia considerably larger than  $\mathcal{J}_{\text{rig}}$ . Similarly, in some parametrisations of the Woods–Saxon potential, the radius parameter is different from experimentally observed nuclear radii and, with  $\mathcal{J} \propto r^2$ , this might have rather drastic effects.

It is expected, however, that the *fluctuations* are more accurately described by the sums, cf. chapter 9. Therefore, it appears reasonable to retain only these fluctuations with the average behaviour governed by the rigid body moment of inertia. To this end we define (see e.g. Andersson *et al.*, 1976) a spin-dependent shell correction energy

$$E_{\text{sh}}(I_0) = \sum e_i \left|_{I=I_0} - \widetilde{\sum e_i} \right|_{I=I_0}$$

where the smoothed single-particle sums (indicated by ‘~’) are calculated from a Strutinsky procedure essentially the same as that described in chapter 9. Subsequently, the total energy is calculated as the sum of the rotating liquid-drop energy and the shell energy,

$$E_{\text{tot}}(\bar{\varepsilon}, I) = E_{L.D.}(\bar{\varepsilon}, I=0) + \frac{\hbar^2}{2\mathcal{J}_{\text{rig}}(\bar{\varepsilon})} I^2 + E_{\text{sh}}(\bar{\varepsilon}, I)$$

where  $\bar{\varepsilon}$  is a shorthand notation for the deformation,  $\bar{\varepsilon} = (\varepsilon, \gamma, \varepsilon_4, \dots)$ .

In the definition of the shell energy, all quantities should be evaluated at the same spin  $I_0$ , i.e. the smoothed single-particle energy sum should be calculated at an  $\omega$ -value giving a smoothed spin  $\widetilde{\sum m_i} = I_0$ . Thus, the  $\omega$ -values in the discrete sum and in the smoothed sum are generally different and it becomes difficult to get any feeling for the variation of  $E_{\text{sh}}$  from an inspection of a single-particle diagram. However, it can be shown that the quantity

$$E_{\text{quasi-sh}}(\omega) = \sum e_i^\omega - \widetilde{\sum e_i^\omega}$$

with all quantities calculated at the same  $\omega$  is numerically very similar to  $E_{\text{sh}}$ . An elementary discussion of this is given in Ragnarsson *et al.* (1978). The quantity  $E_{\text{quasi-sh}}$  is defined exactly analogous to the static shell energy discussed in chapter 9. Thus,  $\omega$  enters very much as a deformation parameter and we can take over all our experience from the static case; specifically that gaps in the single-particle spectrum give a favoured (negative) shell energy while a large level density leads to a positive shell energy, i.e. an unfavoured configuration.

## 12.6 Competition between collective and single-particle degrees of freedom in medium-heavy nuclei

We will now turn to heavier nuclei where, as seen in fig. 11.2, the moment of inertia extracted from the measured  $2^+$  to  $0^+$  energy spacing is less than 50% of the calculated rigid body value. We have already pointed out that the low value is due to the pairing correlations (the pairing correlations are less important in a light nucleus like  $^{20}\text{Ne}$ ). With increasing spin, the experimental moment of inertia becomes larger (fig. 11.13) and for the deformed rare-earth nuclei, it comes close to the rigid body value in the  $I = 20\text{--}30$  region. This suggests that the pairing correlations are rather unimportant at these spins and the same conclusion is also reached from more fundamental theoretical considerations. The cranking model in the form in which we applied it to  $^{20}\text{Ne}$ , with independent particles in a rotating potential, should then be applicable to heavy nuclei at high enough spins, let's say  $I \geq 30$ . For such high spins, the approximation of identifying the total spin with the projection on the rotation axis should also be quite accurate. The result from  $^{20}\text{Ne}$  that the model seems to describe the spectrum quite reasonably all the way down to  $I = 0$  or at least  $I = 2$  is in some ways surprising. Indeed, the application of a rotating independent particle model to the  $I = 0, 2, \dots$  states of  $^{20}\text{Ne}$  can hardly be justified theoretically.

Calculated potential energy surfaces for  $^{160}\text{Yb}$  at different spin values

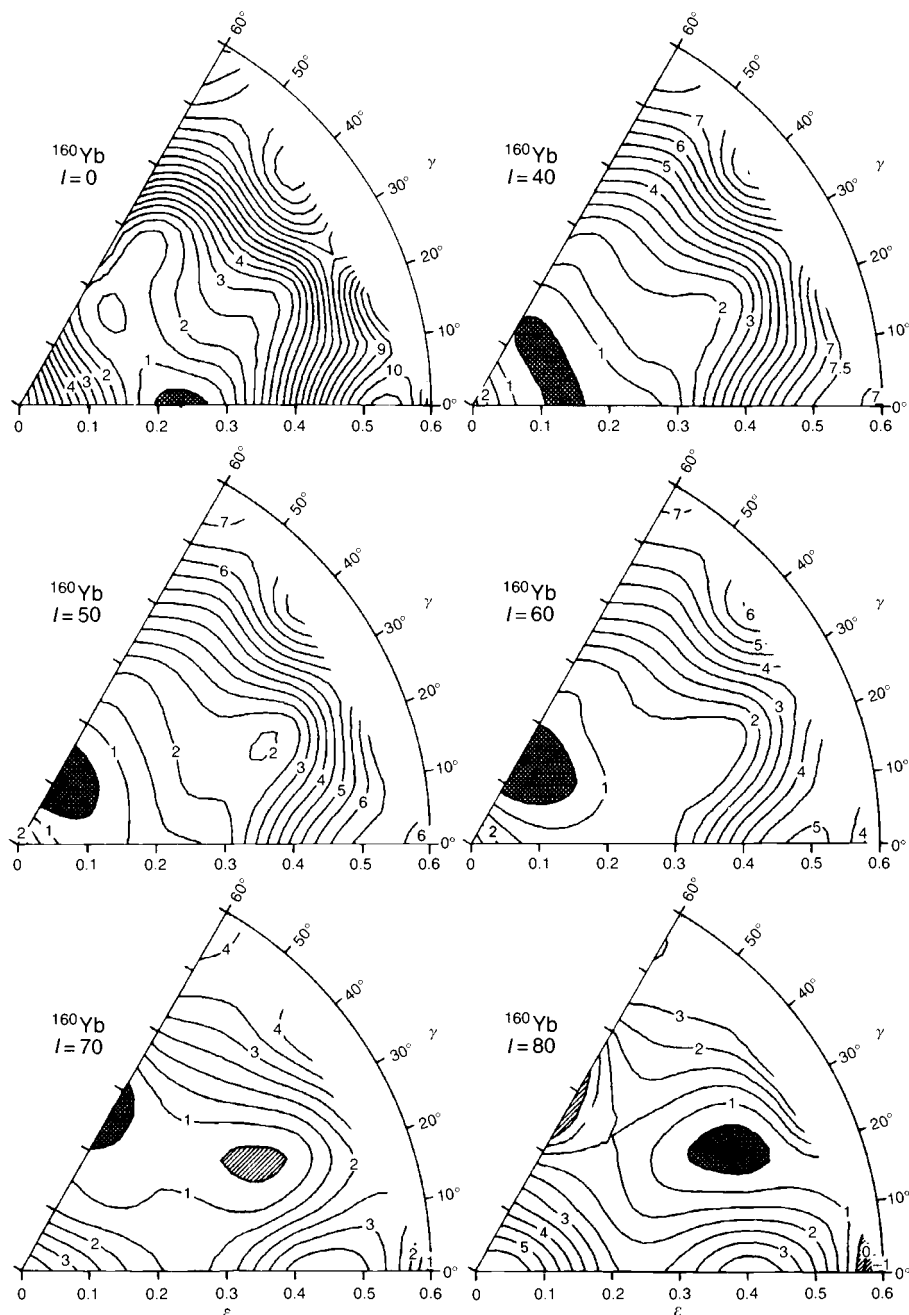


Fig. 12.8. Calculated  $I = 0, 40, 50, 60, 70$  and  $80$  potential energy surfaces in the  $(\epsilon, \gamma)$  plane with inclusion of the shell energy for  $^{160}_{70}\text{Yb}_{90}$ . The contour line separation is 1 MeV (from Andersson *et al.*, 1976).

are exhibited in fig. 12.8. The nucleus is prolate for  $I = 0$  but becomes soft toward  $\gamma = 60^\circ$ , with increasing spin. At  $I = 50$ , a shape transition has occurred and the lowest energy is found for oblate shape with rotation around the symmetry axis ( $\gamma = 60^\circ$ ). The same general trend as in  $^{20}\text{Ne}$  is thus obtained. However, the difference in mass means that the large shape transitions occur at very different spins,  $I = 8$  in  $^{20}\text{Ne}$  compared with  $I = 40\text{--}50$  in  $^{160}\text{Yb}$ .

The energy surfaces of fig. 12.8 should be understood as some average of the states in the yrast region at the different spin values exhibited. If the different states are considered in more detail (Bengtsson and Ragnarsson, 1985), it turns out that the shell effects leading to the  $\gamma = 60^\circ$  shape transition are very similar to those in  $^{20}\text{Ne}$ . Thus, at high spins,  $^{160}\text{Yb}$  can be considered as a closed core of  $^{146}\text{Gd}$  and 14 additional valence particles in the  $j$ -shells above the  $Z = 64$  and  $N = 82$  shell closures. (See figs. 11.5 and 11.6 where one notes that the  $Z = 64$  gap is smaller than e.g. the  $Z = 50$  and  $Z = 82$  gaps, and it is only for nuclei with a limited number of valence nucleons outside the  $^{146}\text{Gd}$  core that it shows any magic properties (Kleinheinz *et al.*, 1979).) For example, according to calculations for  $^{160}\text{Yb}$ , it is possible to define a configuration with six  $h_{11/2}$  valence protons, six valence neutrons distributed over the  $f_{7/2}$  and  $h_{9/2}$  shells and the remaining two neutrons in the  $i_{13/2}$  shell. In this configuration denoted  $\pi(h_{11/2})^6\nu(f_{7/2}h_{9/2})^6(i_{13/2})^2$ , it is possible to follow the gradual alignment of the spin vectors until full alignment in an  $I^\pi = 48^+$  state where the  $h_{11/2}$  protons contribute with 18 spin units ( $11/2 + 9/2 + 7/2 + 5/2 + 3/2 + 1/2$ ), the  $f_{7/2}$  and  $h_{9/2}$  neutrons also with 18 spin units ( $9/2 + 7/2 + 7/2 + 5/2 + 5/2 + 3/2$ ) and the  $i_{13/2}$  neutrons with 12 spin units ( $13/2 + 11/2$ ). Similarly, it is for example possible to form a  $46^+$  terminating state in  $^{158}\text{Er}$  from the configuration  $\pi(h_{11/2})^4\nu(f_{7/2}h_{9/2})^6(i_{13/2})^2$  and a  $42^+$  terminating state in  $^{156}\text{Er}$  from the configuration  $\pi(h_{11/2})^4\nu(f_{7/2}h_{9/2})^4(i_{13/2})^2$ .

The labelling of the configurations would be somewhat easier if all the  $j$ -shells could be considered as essentially pure and thus distinguishable. However, at typical ground state deformations of  $\epsilon \geq 0.2$ , the neutron  $h_{9/2}$  and  $f_{7/2}$  shells are rather strongly mixed (see fig. 11.6). Therefore, in our labelling we have considered these two subshells as one unit. On the other hand, at the termination, which generally occurs at  $\epsilon \approx 0.1$  ( $\gamma = 60^\circ$ ), the two shells are more pure and then it seems justified for example to refer to the  $\nu(f_{7/2}h_{9/2})^6$  structure as three  $f_{7/2}$  neutrons coupled to  $(15/2)\hbar$  and three  $h_{9/2}$  neutrons coupled to  $(21/2)\hbar$ .

Starting from the configurations mentioned above, other terminating bands can be formed for example by redistributing the neutrons among the  $(f_{7/2}h_{9/2})$

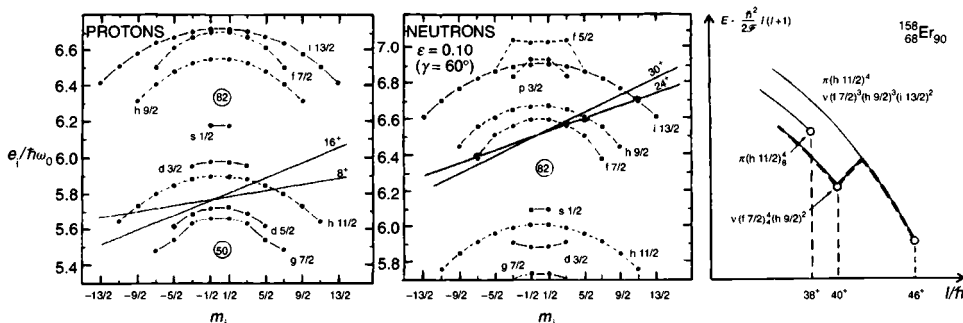


Fig. 12.9. Single-particle energies  $e_i$  for oblate shape,  $\varepsilon = 0.10$ , versus spin projection on the symmetry axis  $m_i$  together with a schematic illustration of the band structure in the closed core configuration of  $^{158}\text{Er}$ . Sloping Fermi surfaces indicate the filling of the orbitals in the fully aligned  $I_p = 16$  and  $I_n = 30$  states and also in the cases of one proton and neutron, respectively, anti-aligned giving  $I_p = 8$  and  $I_n = 24$  states. It then becomes possible to form energetically favoured  $46^+$ ,  $40^+$ ,  $38^+$  and  $32^+$  states, each associated with a terminating band as illustrated for the three higher spin values in the right part of the figure where the  $40^+$  state is assumed yrast and the  $38^+$  state is not. With no interaction, between the bands, an yrast line as shown by the thick dashed line results. Similarly, a sloping Fermi surface giving  $I_n = 33^-$  can be drawn so that for example a favoured  $49^-$  state might be formed (from Ragnarsson *et al.*, 1986).

and  $i_{13/2}$  shells or by making holes in the proton core. Thus, in  $^{158}\text{Er}$  we expect for example a  $\pi(d_{5/2})^{-1}(h_{11/2})^5\nu(f_{7/2}h_{9/2})^5(i_{13/2})^3$  configuration terminating in a  $53^+$  state and so on. It also seems possible to define band-terminating states where one spin vector points in the opposite direction relative to the total spin vector. As one example, consider an oblate  $\pi(h_{11/2})^4\nu(f_{7/2})^4(h_{9/2})^2(i_{13/2})^2$  configuration in  $^{158}\text{Er}$  where one of the  $f_{7/2}$  neutrons gives a spin contribution of  $(-7/2)\hbar$ , i.e. the four  $f_{7/2}$  neutrons contribute only with  $(7/2 + 5/2 + 3/2 - 7/2)\hbar = 4\hbar$ , while the nucleons in the other subshell contribute with their maximal possible spin. The  $f_{7/2}$  ( $\Omega = m = \pm 7/2$ ) orbital is thus occupied by two particles, which can be understood from the fact that, at the oblate deformation in question, this orbital is far below the Fermi surface (see fig. 8.3 where the orbital is labelled [514 7/2] ( $\varepsilon < 0$ )).

As discussed already for the sd-shell nuclei, a more quantitative comparison between different aligned configurations is obtained from  $e_i$  versus  $m_i$  diagrams drawn at the appropriate deformation. This is illustrated for  $^{158}\text{Er}$  in fig. 12.9 where some corresponding terminating bands are also shown schematically. Similarly, we show in fig. 12.10 how the neutron configuration of  $^{158}\text{Er}$ ,  $(f_{7/2}h_{9/2})^6(i_{13/2})^2$ , can be followed from the ground state to the terminating configuration with a neutron spin of  $30\hbar$ . Other terminat-

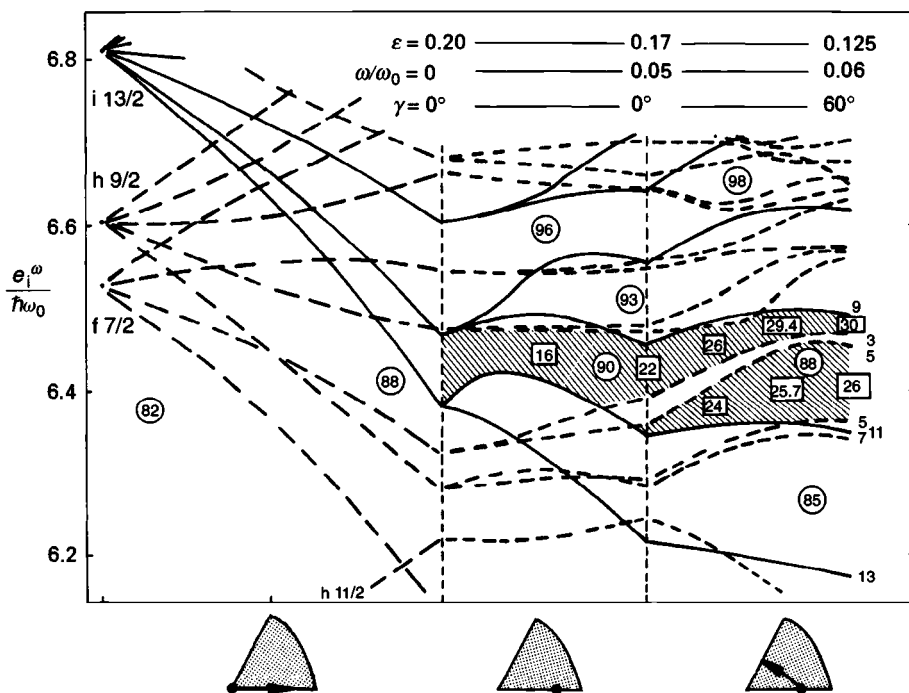


Fig. 12.10. Similar to fig. 12.4 but for neutrons around  $N = 90$ . Thus the left panel illustrates the spherical origin of the ground state orbitals while the other two panels show the orbitals in the  $(\varepsilon, \varepsilon_4, \gamma, \omega)$  plane along an approximate path to termination. Particle numbers are given within rings and total neutron spin at specific deformations and rotational frequencies within rectangles. At the termination for oblate shape (right edge of the figure), twice the spin projection on the symmetry axis,  $2m_i$ , is indicated for some orbitals. It is interesting to note how the  $N = 90$  gap survives all the way to the termination while a large  $N = 88$  gap develops close to the termination.

ing neutron configurations are then obtained as particle–hole configurations with respect to this optimal configuration. Which configuration is considered optimal might, however, depend on the specific deformation and rotational frequency chosen.

The structure of  $^{20}\text{Ne}$  is particularly simple because the ground state configuration is identical to the configuration terminating for  $I^\pi = 8^+$ . Fig. 12.10 shows that the situation is similar for the  $N = 90$  neutron configuration. For the protons in the  $A \approx 160$  nuclei on the other hand the terminating configurations come into the yrast region first for spin values in the  $I = 30\text{--}40$  region while, at lower spins, other configurations are yrast. For example, from figs. 11.5 and 11.6, we may conclude that an approximate ground state configuration of  $^{158}\text{Er}$  ( $\varepsilon \approx 0.20$ ) is of the

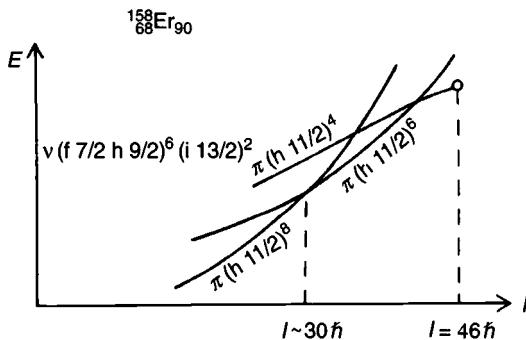


Fig. 12.11. Schematic illustration of the proton configuration yrast bands in  $^{158}\text{Er}$ . As seen in fig. 11.5, in the ground state there are 8 protons in  $h_{11/2}$  orbitals but with increasing spin, there is a tendency to close the  $Z = 64$  core and thus to ‘de-excite’ protons from the  $h_{11/2}$  shell above the gap to the  $d_{5/2}$  and  $g_{7/2}$  shells below the gap. In the configuration with all shells below the  $Z = 64$  gap filled ( $h_{11/2})^4$ , an energetically favoured termination occurs for  $I = 46$ . In this aligned state, the spin contribution is  $16\hbar$  from the protons and  $30\hbar$  from the neutrons. As seen in fig. 12.10, the neutrons remain in the same configuration,  $\nu(f_{7/2} h_{9/2})^6 (i_{13/2})^2$ , for all spins up to the termination (from Ragnarsson *et al.*, 1986).

form  $\pi(d_{5/2}g_{7/2})^{-4}(h_{11/2})^8\nu(f_{7/2}h_{9/2})^6(i_{13/2})^2$ . Then with increasing spin, the deformation will develop towards decreasing  $\epsilon$ -deformation and increasing  $\gamma$ -deformation leading to a band-crossing so that the configuration with two protons moved from  $h_{11/2}$  to  $(d_{5/2}g_{7/2})$  comes lower in energy before, at even higher spins, we reach the band-terminating configuration discussed above with a closed  $Z = 64$  core. This situation is schematically illustrated in fig. 12.11. There we have omitted the low spin region, partly to indicate that at these spins the discussion above is only qualitatively but not quantitatively correct because of the neglect of pairing in the calculations. Note also that in each step two protons are exchanged between positive and negative parity orbitals in order to preserve the total parity.

Calculated potential energy surfaces close to termination in the  $\pi(h_{11/2})^4\nu(f_{7/2}h_{9/2})^6(i_{13/2})^2$  configuration of  $^{158}\text{Er}$  are shown in fig. 12.12 while calculated energies for different configurations are compared in fig. 12.13. In fig. 12.14 the calculated evolution with shape of these different configurations is depicted. The bands denoted 1, 2 and 3 in figs. 12.13 and 12.14 are identical to the three bands shown schematically in fig. 12.11. The other bands then correspond to a redistribution of the valence nucleons over the open  $j$ -shells and/or making one or several holes first in the proton  $Z = 64$  core and then also in the neutron  $N = 82$  core.

With a fixed distribution of the particles over the  $j$ -shells, all configu-

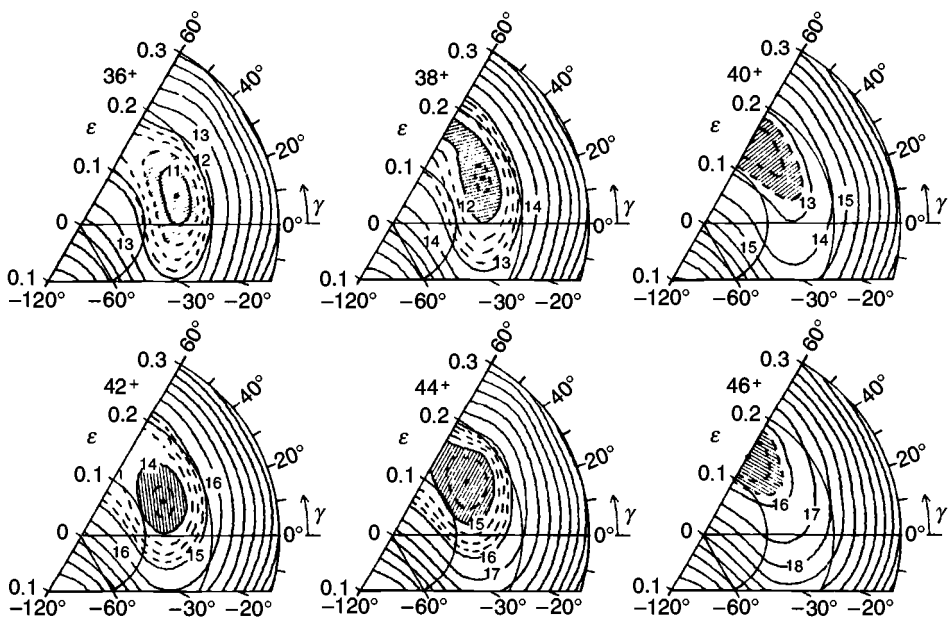


Fig. 12.12. Calculated potential energy surfaces for  $^{158}\text{Er}$  in the configuration that terminates for  $I = 46$ . The configuration for the particles outside the  $Z = 64$  and  $N = 82$  cores is  $\pi(h_{11/2})^4\gamma(f_{7/2}h_{9/2})^6(i_{13/2})^2$  where the  $f_{7/2}$  and  $h_{9/2}$  shells are mixed so that no distinction can be made between neutrons in one or the other of these subshells. This means for example that the ‘two configurations’ terminating at  $I = 40$  and  $I = 46$  in fig. 12.9 are both considered and the minimum is found at oblate shape ( $\gamma = 60^\circ$ ) for these two spins (from Ragnarsson *et al.*, 1986).

rations will terminate sooner or later. However, it seems that it is only configurations with a few particles (or holes) distributed over rather many high- $j$  subshells that are favoured in energy at the termination. Alternatively, this could be expressed by the fact that all valence particles should give an appreciable contribution to the total spin. Therefore, for example an  $(h_{11/2})^6$  configuration does not really favour a termination because the two last protons give a spin contribution of only  $(1/2 + 3/2)\hbar$  in the terminating state. For an  $(h_{11/2})^8$  configuration the two last protons give a negative spin contribution and the (oblate) terminating state is even less favoured. One further observation is that particles rotating around the equator tend to make the nucleus oblate while holes of corresponding type will ‘dig a hole’ at the equator, thus trying to make the nucleus prolate (with ‘rotation around the symmetry axis’, i.e.  $\gamma = -120^\circ$ ). For example, coming back to the  $(h_{11/2})^8$  configuration, it could as well be described as a  $(h_{11/2})^{-4}$  configuration relative to a filled shell and combined with other high- $j$  hole

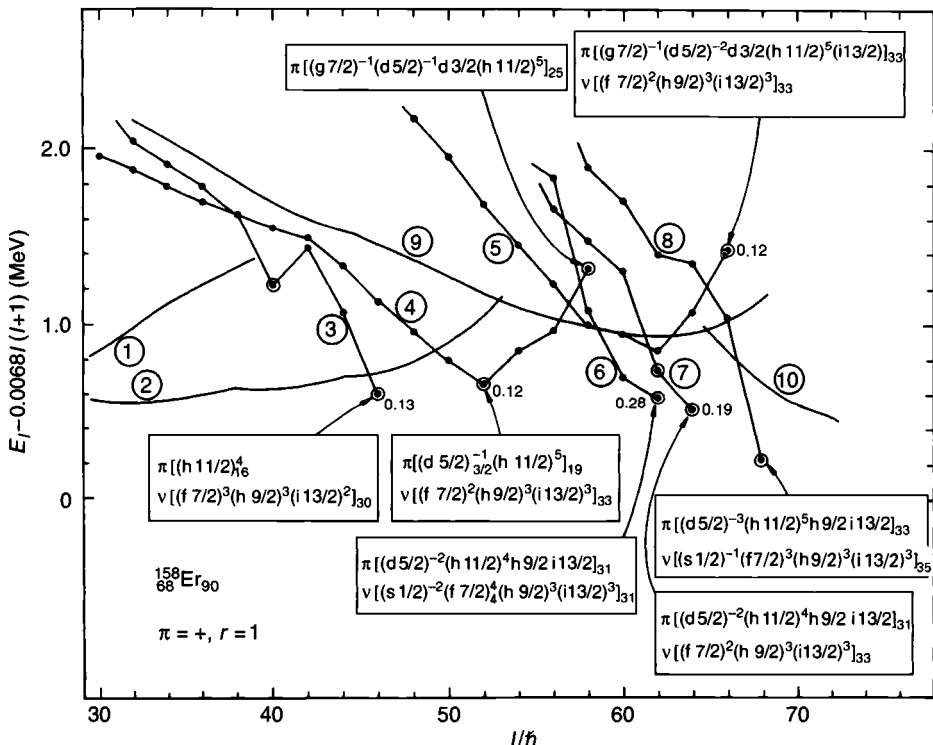


Fig. 12.13. Calculated energies of rotational bands in the yrast region of  $^{158}\text{Er}$ . The bands labelled by 1, 2 and 3 are identical to the three bands of fig. 12.11. An open circle indicates an oblate aligned state ( $\gamma = 60^\circ$ ). For most such oblate states, the configuration relative to a  $^{146}\text{Gd}$  core and the deformation  $\epsilon$  is given (from Bengtsson and Ragnarsson, 1983).

configurations, a favoured prolate band-termination might be formed. Note, however, that high- $j$  hole states and high- $j$  particle states strive in opposite directions and therefore do not live very well together.

In figs. 12.13 and 12.14, we observe a mixture of bands which terminate and which essentially stay collective for all spins. The latter is the case not only for bands 1 and 2 but also for band 9, which is calculated as yrast or close-to-yrast in the  $I = 50\text{--}60$  region. At these spins, one will also note that the centrifugal effects favouring larger deformations become more important and as suggested for example from fig 12.8 and discussed in the next section, some strongly deformed minima may come lowest in energy.

It seems that the calculated features discussed above are surprisingly well borne out in experiment. Thus, the observed (Simpson *et al.*, 1984, Tjøm *et al.*, 1985)  $\gamma$ -ray energies of  $^{158}\text{Er}$  shown in fig. 11.12 are consistent with

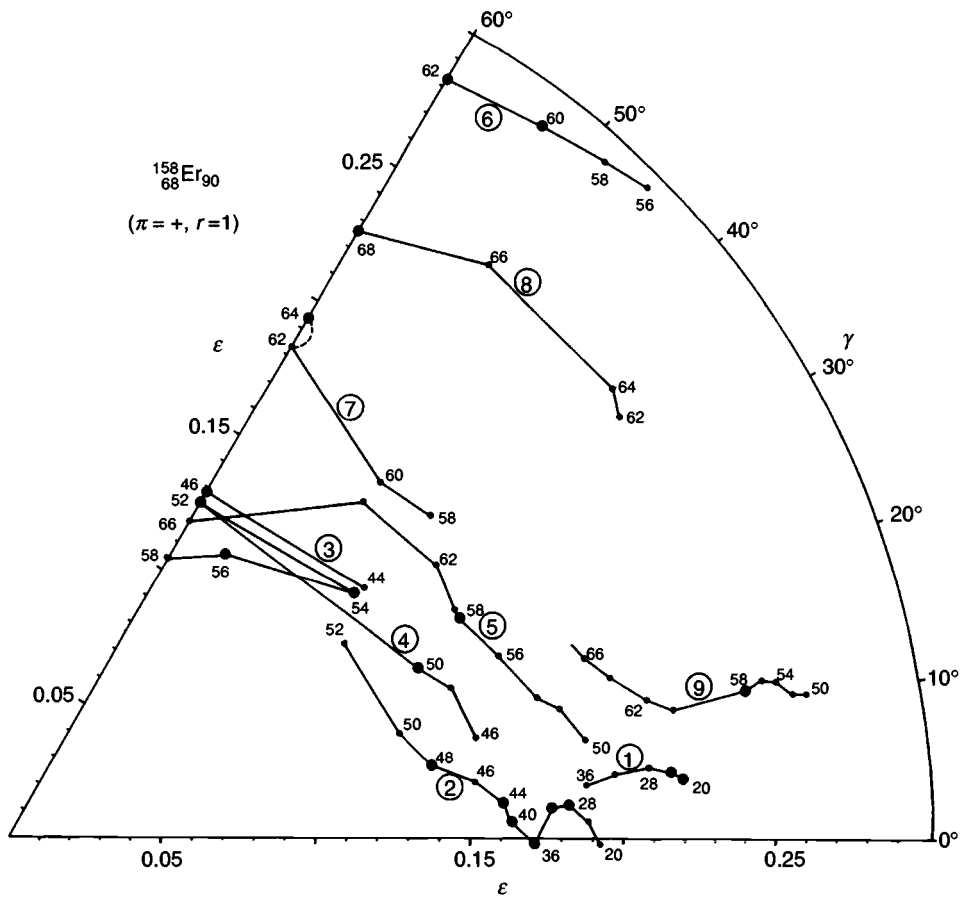


Fig. 12.14. Calculated shape trajectories for different rotational bands in the yrast region of  $^{158}\text{Er}$ . The bands are labelled as in fig. 12.13 and the yrast states denoted by large filled circles. The configuration of some other bands can be extracted from the structure of the band-terminating states given in fig. 12.13 (from Bengtsson and Ragnarsson, 1983).

a crossing between bands 2 and 3 of fig. 12.13 at  $I \approx 40$ , which should be compared with  $I \approx 44$  in the calculations. With a small adjustment of the single-particle parameters, we might even get full agreement. Evidence for band terminations has also been found in  $^{158}\text{Yb}$  (Baktash *et al.*, 1985, Ragnarsson *et al.*, 1985) and  $^{156}\text{Er}$  (Stephens *et al.*, 1985). In the latter nucleus, the positive parity ground band is collective up to  $I \approx 30$  but around this spin, the spectrum changes character with somewhat irregular and comparatively small transition energies. Thus, when plotted as in fig. 12.13 relative to a rigid-rotation energy, the  $I = 30\text{--}42$  structure comes down in

energy with the  $42^+$  state very low-lying as predicted for a terminating state (Ragnarsson *et al.*, 1986). Indeed,  $I^\pi = 42^+$  is identical to the maximum spin in the expected yrast configuration  $\pi(h_{11/2})^4\nu(f_{7/2}h_{9/2})^4(i_{13/2})^2$ . Note also the large gap associated with this neutron configuration to the far right in fig. 12.10.

Here, we have mainly discussed the nuclei with valence particles outside the  $^{146}\text{Gd}$  core. However, starting from other closed shell nuclei similar analyses could be carried through and, as indicated above, also for holes in a closed core, an analogous formalism should be valid. The nuclei we have discussed here with  $A \approx 160$  are, however, especially advantageous for several reasons. From the experimental side it is so because they are neutron deficient, which makes it easy to form high spin states from heavy ion reactions (fig. 11.11). Furthermore, nuclei with mass numbers  $A = 100\text{--}200$  on the average can accommodate the highest spins as seen from fig. 12.3. From the theoretical side, the presence of several high- $j$  shells just above the  $Z = 64$  and  $N = 82$  shell closures make the terminating bands especially favoured.

## 12.7 Shell effects at large deformation

In the preceding section, we discussed the case of a few valence nucleons outside closed shells leading to states of single-particle character at intermediate spin values. With more particles outside the core, the nucleus will stay collective to higher spins with only small shape changes. In any case, however, the centrifugal force will sooner or later become dominating as discussed within the liquid-drop model above and illustrated in figs. 12.2 and 12.3. Indeed, for nuclei with mass  $A = 100\text{--}150$ , the liquid-drop energy will be very soft over large regions of the deformation plane for spins  $I \approx 50\text{--}60$ . This means that the shell effects may play a very important role, creating minima at small but also at large and very large deformations. One example of this is seen for  $^{160}\text{Yb}$  in fig. 12.8 where a minimum develops for  $\epsilon \approx 0.4$  and  $\gamma = 20\text{--}30^\circ$ .

Because of the important role of the shell effects, it seems appropriate to consider their properties at large deformation in some detail. In general, one expects larger shell effects for axial symmetric shapes than for triaxial shapes. In the static harmonic oscillator approximation, this is understood from the fact that the quanta in the two perpendicular directions can be interchanged with no change in the single-particle energies. Consequently, large degeneracies occur as indicated in fig. 8.1. For example, with a two-fold spin degeneracy, the  $n_z = 0$  orbitals with all quanta in the perpendicular

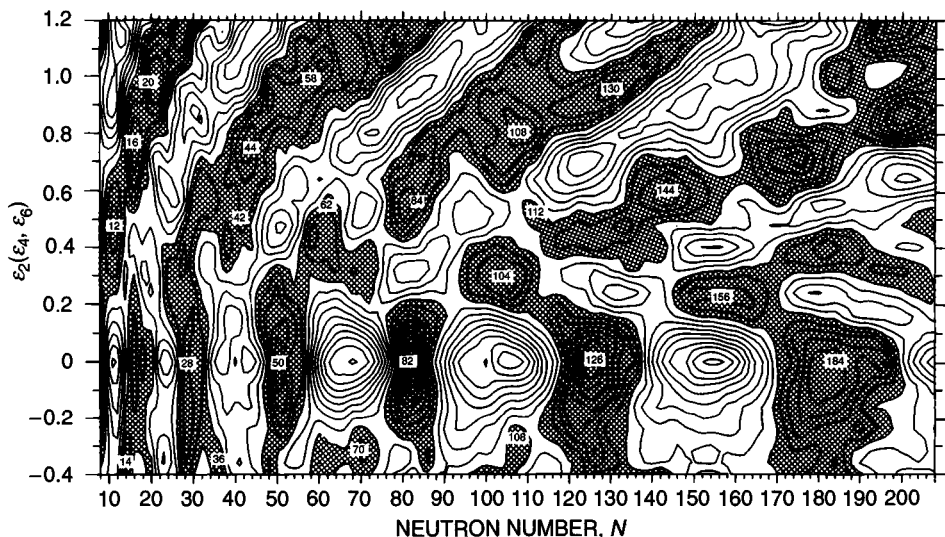


Fig. 12.15. The shell energy landscape for neutrons drawn as a function of neutron number and elongation. The shell energy is negative in shaded regions and the contour line separation is 1 MeV. Some neutron numbers in regions of favoured shell energy are indicated. The magic numbers for spherical shape are seen clearly. Another very prominent feature of the plot are the ridges that intersect the landscape, bending towards higher particle numbers with increasing prolate deformation. These ridges are caused by the numerous  $n_z = 0$  orbitals, which are degenerate in the pure oscillator. In between the ridges, regions of negative shell energy are seen, suggesting very definite relationships between particle number and deformation for favoured configurations at large deformation (from I. Ragnarsson and R.K. Sheline, 1984, *Phys. Scripta* **29**, 385).

direction have a total degeneracy of  $2(N + 1)$  while those with one quantum in the polar direction ( $n_z = 1$ ) have a total degeneracy of  $2N$ . In more realistic potentials like the modified oscillator, the  $n_z = 0$  and  $n_z = 1$  orbitals are not degenerate but most of them are still rather close together, see figs 8.2 and 8.5. In the latter figure, the regions of dense shading correspond to the  $n_z = 0$  orbitals and those with less dense shading to  $n_z = 1$  orbitals. Note that the orbitals emerging from the high- $j$  intruder shells do not fit into this scheme as they are far below the other orbitals with the same  $n_z$  and  $n_\perp$ . An example seen in figs. 8.2 and 8.5 is the [505 11/2] orbital from the  $N = 5$   $h_{11/2}$  subshell. The approximate degeneracy of the low- $n_z$  orbitals is thus not applicable to the full oscillator spectrum as discussed by Ragnarsson *et al.* (1978). This has also been noted in the analysis of the Woods–Saxon potential by Dudek *et al.* (1987), who introduced the term pseudo-oscillator symmetry.

A more quantitative measure of the approximate degeneracies of the single-particle orbitals is obtained if the shell energy is plotted as a function of particle number and elongation, see fig. 12.15. Consider as an example the  $n_z = 0, N = 5$  orbitals (fig. 8.5), which are found at the Fermi level for  $N \approx 100$  at spherical shape,  $N \approx 135$  at  $\varepsilon = 0.3$  and  $N \approx 185$  at  $\varepsilon = 0.6$ . The high level density along this path should then lead to a ridge of unfavourable positive shell energy, which is indeed the case. In a similar way, other ridges are created in fig. 12.15 from the  $n_z = 0, N = 4$  orbitals, etc. while the approximate degeneracies of the  $n_z = 1$  orbitals almost appear too small to give any discernible ridges in fig. 12.15.

In between the regions of high level density, there will by necessity be fewer single-particle orbitals leading to valleys in the shell energy landscape. This corresponds to a favoured shell energy, which is really what we are looking for. Thus, it is suggested from fig. 12.15 that the regions of low shell energy occur in a very regular and well-defined way at large prolate deformations. Furthermore, this general structure is the same for protons as for neutrons.

The feature of the harmonic oscillator spectrum that has been discussed most in the literature (e.g. Bohr and Mottelson, 1975 and references therein) is the large degeneracies that occur when all three frequencies are related through

$$\omega_x : \omega_y : \omega_z = a : b : c$$

where  $a, b, c$  are small integer numbers. Apart from spherical shape ( $1 : 1 : 1$ ) the most important ratios seen in fig. 8.1 correspond to  $\omega_{\perp} : \omega_z = 2 : 1$  (cf. problem 5.1) and  $\omega_{\perp} : \omega_z = 1 : 2$ . In fig. 12.15, the prolate  $2 : 1$  ratio shows up in the form of somewhat increased shell effects for  $\varepsilon \approx 0.6$  compared with for other prolate shapes.

Note also that minima at  $\varepsilon \approx 0.6$  (fig. 12.15) are seen at somewhat larger particle numbers than the shell gaps of the pure oscillator (fig. 8.1). For example, shell gaps at  $N = 60$  and  $80$  correspond to a favoured shell energy of the modified oscillator at  $\varepsilon \approx 0.6$  for  $N \approx 60\text{--}66$  and  $N \approx 80\text{--}88$ . As illustrated in fig. 8.2 this is understood from the way the orbitals are influenced by the  $\ell^2$ -term and to a smaller extent by the  $\varepsilon_4$ -term. It seems rather well established that the fission isomers discussed in chapter 9 show up because of a large negative shell energy for  $\varepsilon \approx 0.6$  and  $N = 140\text{--}150$  (fig. 12.15).

Fig. 12.15 is drawn for a static potential. The question is now what happens for a rotating potential. Indeed, the rotation will only influence the shell structure in a minor way (e.g. Ragnarsson *et al.*, 1980). The reason is

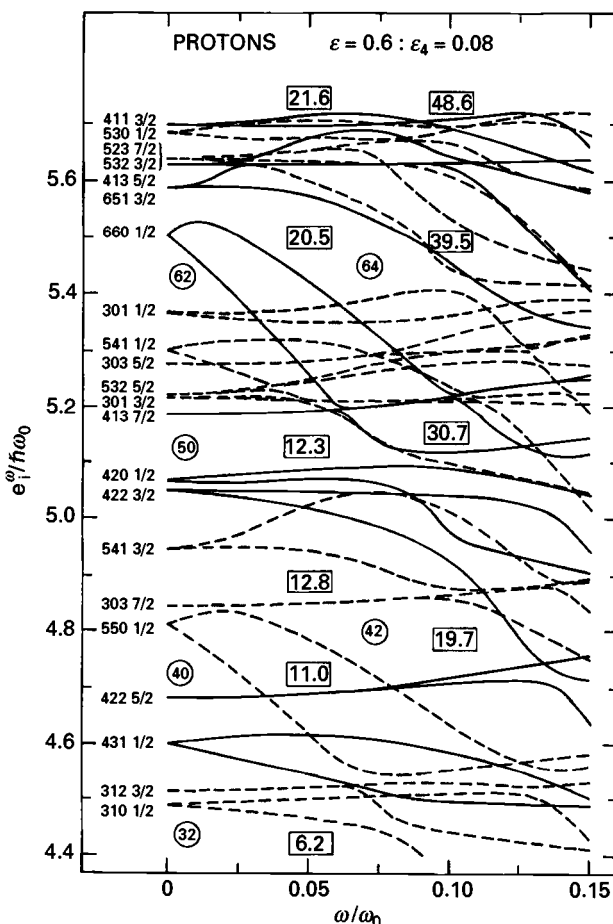


Fig. 12.16. The single-proton orbitals of the modified oscillator potential plotted as functions of rotational frequency. The deformation,  $\varepsilon = 0.6$  corresponds to a 2 : 1 ratio of the symmetry axis and the perpendicular axis. The orbitals are labelled by the asymptotic quantum numbers at  $\omega = 0$ . At frequencies  $\omega/\omega_0 = 0.05$  and 0.10, total spins for different particle numbers (shown in rings) are given within rectangles. Note that most orbitals are only weakly dependent on rotational frequency so that the regions of low and high level density are very little disturbed by the rotation (from Ragnarsson *et al.*, 1980).

that the rotation is strongly collective so that many orbitals contribute to the angular momentum but each orbital only marginally. Therefore, most orbitals get only a small  $\langle j_x \rangle$  corresponding to a small slope in fig. 12.16 where the proton orbitals at  $\varepsilon = 0.6$  are drawn. Orbitals having a small  $n_z$  are especially difficult to align. However, according to the discussion above, these are the orbitals that are essentially responsible for the regularity in

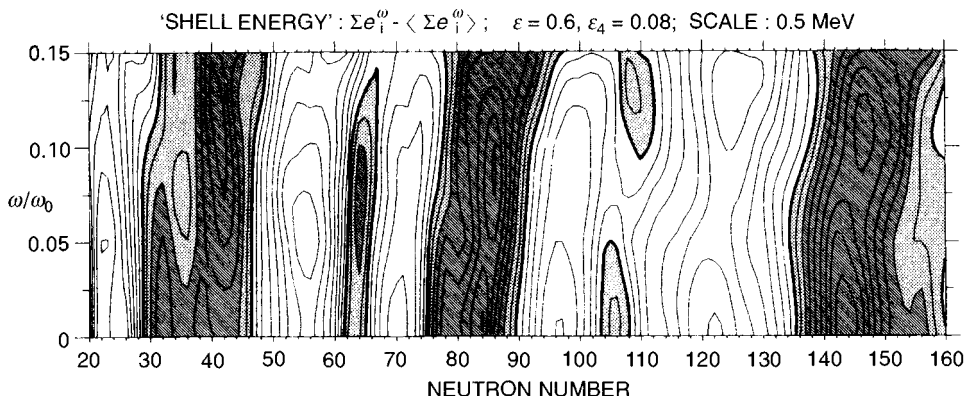


Fig. 12.17. The neutron shell energy drawn versus particle number and rotational frequency. The corresponding proton diagram is quite similar and as suggested from fig. 12.16, favoured particle numbers remain constant or are only slightly shifted at rapid rotation (from S. Åberg *et al.*, *Proc. Fourth IAEA Symp. on Phys. and Chem. of Fission*, Jülich, 1979 (IAEA, Vienna, 1980) vol. I, p. 303).

the shell effects. The fact that a few high- $n_z$  (and high- $N$ ) orbitals get a stronger alignment does not alter the shell structure in any major way. This becomes evident from fig. 12.17 where the calculated neutron shell energy at  $\varepsilon = 0.6$  is shown as a function of neutron number  $N$  and rotational frequency  $\omega$ . It is evident that particle numbers of favoured and unfavoured shell energies are essentially the same independent of  $\omega$ . This is apart from a general tendency that the valleys of favoured shell energy are slightly shifted towards higher particle numbers with increasing  $\omega$ . This small shift is easily understood from the way in which the few orbitals showing strong alignment in fig. 12.16 cut through the large number of 'less aligned' orbitals. Note also that fig. 12.16 is drawn for protons while fig. 12.17 is drawn for neutrons. Even so the same particle numbers are favoured in both cases, e.g.  $Z = 62\text{--}64$  in fig. 12.16 and  $N = 62\text{--}64$  in fig. 12.17. This underlines once more that the main features of the shell effects are governed by the general symmetries and not by the detailed features of the single-particle potential. Therefore these main features are the same for protons as for neutrons.

## 12.8 Rotational bands at superdeformation

The discussion above suggests that it should be straightforward to obtain superdeformed states at high enough spins in theoretical calculations. This has also been the case with the predictions concentrating on the nuclei



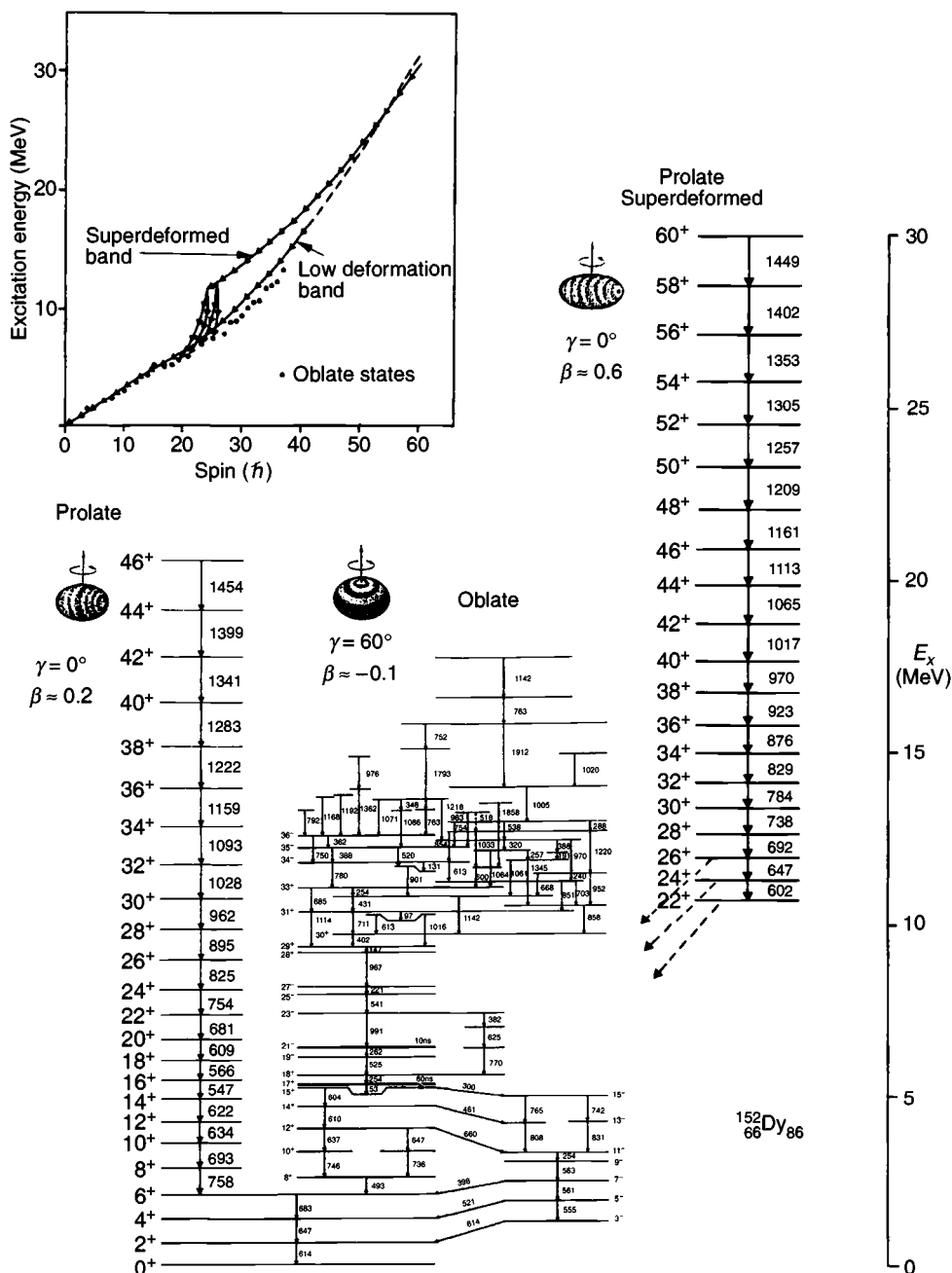


Fig. 12.19. The full spectrum observed for the nucleus  $^{152}\text{Dy}$  showing the low-spin non-collective yrast states in the middle, a collective normal-deformed band to the left and the superdeformed band to the right. The inset in the upper left corner shows  $E$  versus  $I$  plotted in a schematic way for the different structures (from J.F. Sharpey-Schaffer, *Physics World*, Sept. 1990, p. 31).

(and interpreted as slightly oblate). These states are seen at spin  $I \approx 40$ . Furthermore, one collective band corresponding to prolate normal deformation,  $\epsilon = 0.2\text{--}0.3$  is shown at  $I = 46$ . Finally, the superdeformed band extends to  $I \approx 60$  where the exact spin values are not known because it has not been possible to observe the linking transitions between the superdeformed band and the small deformation states.

In many ways, the observed superdeformed band opens a new era in the study of the orbitals and the shell structure at large deformation. From fig. 12.15 it is suggested that favoured shell energies at large deformations are present for more or less all particle numbers but that the favoured deformations are coupled to the particle numbers in a regular pattern. Indeed, since the discovery of the superdeformed band in  $^{152}\text{Dy}$ , several similar rotational bands have been observed in neighbouring nuclei (see Åberg *et al.*, 1990; Janssens and Khoo, 1991, for reviews). Additionally, rotational bands with properties indicating a deformation of  $\epsilon \simeq 0.5$  have been observed in nuclei around  $^{192}_{80}\text{Hg}_{112}$ . It is very satisfying that the proton and neutron numbers do fit into the valleys of fig. 12.15. Also in the nuclei around  $^{132}\text{Ce}$ , several rotational bands with large deformations  $\epsilon = 0.3\text{--}0.4$  have been observed (Nolan and Twin, 1988). Again this is consistent with fig. 12.15 but compared with normal ground state deformations these bands are probably formed by putting one or two particles in deformation driving high- $j$  orbitals, especially in the [660 1/2] neutron orbital. As seen for example in fig. 11.6, this orbital comes down from the next major shell. Therefore, it is questionable whether these states in the Ce/Nd region do increase our knowledge about the shell structure at large deformations in any major way.

From the discussion above, it should be evident that it is mainly the low- $n_z$  orbitals (the equatorial orbitals) that are responsible for the shell structure at large deformation. This feature is independent of rotational frequency. The high- $j$  large- $n_z$  orbitals are, however, very important for the detailed properties of the rotational bands. This is natural because they are the orbitals that are easy to align and which therefore carry a lot of angular momentum. Note that these kinds of orbitals are also responsible for band-crossings in normal-deformed rotational bands or for the polarising forces leading to band terminations.

As discussed in connection with the pure oscillator, a disturbed rotational band can be analysed in the form of different moments of inertia. As the exact spins for the superdeformed bands are not known, it is not possible to extract  $\mathcal{J}^{(1)}$  with any certainty. On the other hand,  $\mathcal{J}^{(2)}$ , which is a measure of the relative change in transition energy, can be calculated from

the relation

$$\mathcal{J}^{(2)}/\hbar^2 = \frac{1}{d^2E/dI^2} \approx \frac{4}{[E_\gamma(I+1) - E_\gamma(I-1)]}$$

where  $E_\gamma(I) = E(I+1) - E(I-1)$  is the transition energy for the transition,  $(I+1) \rightarrow (I-1)$ . When comparing with theory, we note that

$$\mathcal{J}^{(2)}/\hbar^2 = \left( \frac{d^2E}{dI^2} \right)^{-1} = \frac{dI}{d\omega} = \sum_{\text{occ}} \frac{d\langle j_x \rangle}{d\omega}$$

where the last equality is valid in the cranking approximation. Furthermore, we have used the canonical relation,

$$\omega = \frac{dE}{dI}$$

to obtain the rotational frequency from the spectrum. Thus, in the cranking approximation,  $\mathcal{J}^{(2)}$  is a sum from single-particle terms measuring how the alignment  $\langle j_x \rangle$  changes with rotational frequency. It is then instructive to consider how the alignment occurs in a high- $j$  shell, see fig. 12.20 drawn for a  $h_{11/2}$  shell at  $\epsilon = 0.25$ . The general features of this figure remain for other high- $j$  shells and also for larger deformation. At large deformations, however, the different orbitals get aligned at a higher frequency. As  $\mathcal{J}^{(2)}$  measures the increase in alignment, it is evident that the lowest high- $j$  orbital contributes at a very small frequency (fig. 12.20), the next at a somewhat higher frequency and so on.

Realistic calculations illustrating how  $\mathcal{J}^{(2)}$  is built for the superdeformed bands in the  $A \approx 150$  region are shown in fig. 12.21. Note that, for many particles in a shell,  $\mathcal{J}^{(2)}$  is essentially constant similar to what was found in the pure oscillator where no orbital gets a strong alignment. Also, the first, second and third orbitals in a  $j$ -shell contribute as anticipated above. The fourth orbital becomes anti-aligned at low frequencies but it gives a positive contribution to  $\mathcal{J}^{(2)}$  at higher frequencies. This means that, at superdeformation, high- $j$  shells with four particles or more will contribute with an approximately constant value to the  $\mathcal{J}^{(2)}$  moment of inertia.

From the analysis of the observed  $\mathcal{J}^{(2)}$  moment of inertia for the superdeformed bands in  $^{146}_{64}\text{Gd}_{82-66}\text{Dy}_{87}$ , it has been possible to extract probable configurations for most of these bands (Bengtsson *et al.*, 1988, Nazarewicz *et al.*, 1989). The configurations are specified by the number of particles in high- $j$  (or rather high- $N$ ) shells, which according to the discussion above give characteristic contributions to  $\mathcal{J}^{(2)}$ . A large number of superdeformed bands have also been identified in the Hg/Pb region. These nuclei show a very rich structure as indicated from the plot of calculated bands in fig. 12.22.

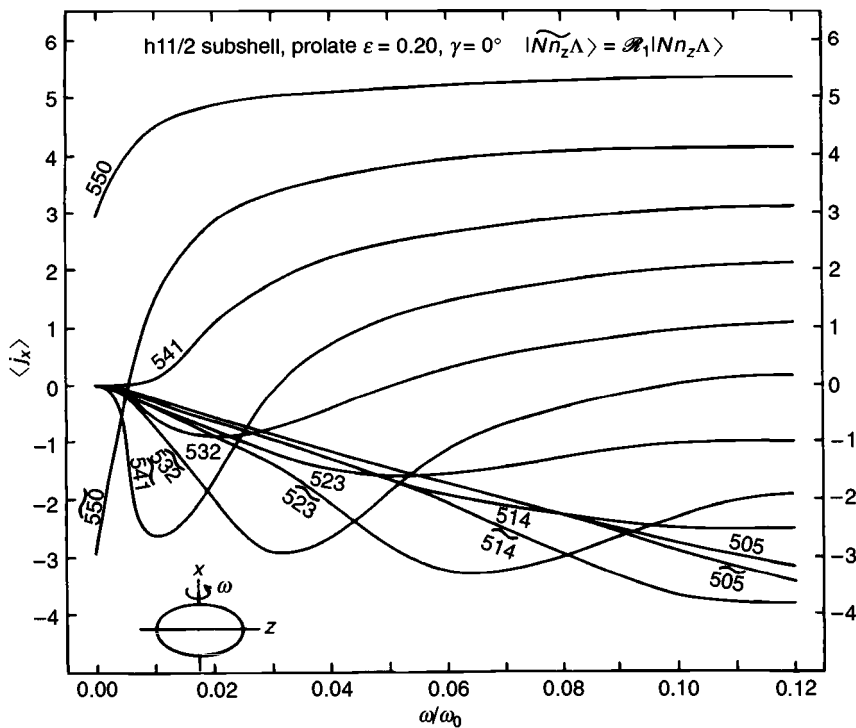


Fig. 12.20. Single-particle angular momentum component along the rotation axis for the  $h_{11/2}$  orbitals at prolate shape,  $\varepsilon = 0.2$ . The orbitals are labelled by their asymptotic quantum numbers. The two-fold degeneracy is broken (cf. fig. 12.16) and the two sets of noninteracting orbitals (having different signature), are drawn with and without a 'tilde'. As discussed also in chapter 11, it is the polar orbitals at the bottom of the shell which become strongly aligned. The figure would be very similar for another high- $j$  shell like  $i_{13/2}$  or  $j_{15/2}$  and it would also be qualitatively unchanged at a larger deformation, however with the alignment becoming more gradual (from Andersson et al., 1976).

Recently, superdeformed rotational bands with identical or almost identical transition energies have been identified in several neighbour nuclei both in the  $A = 150$  and in the  $A = 190$  regions. This has inspired a lot of experimental as well as theoretical investigations so we will discuss it in some more detail.

### 12.9 Identical bands at superdeformation

The first identification of almost identical bands in neighbouring nuclei at superdeformation came very much as a surprise. Indeed, as the spins are not known, what is really known with certainty from experiment is that

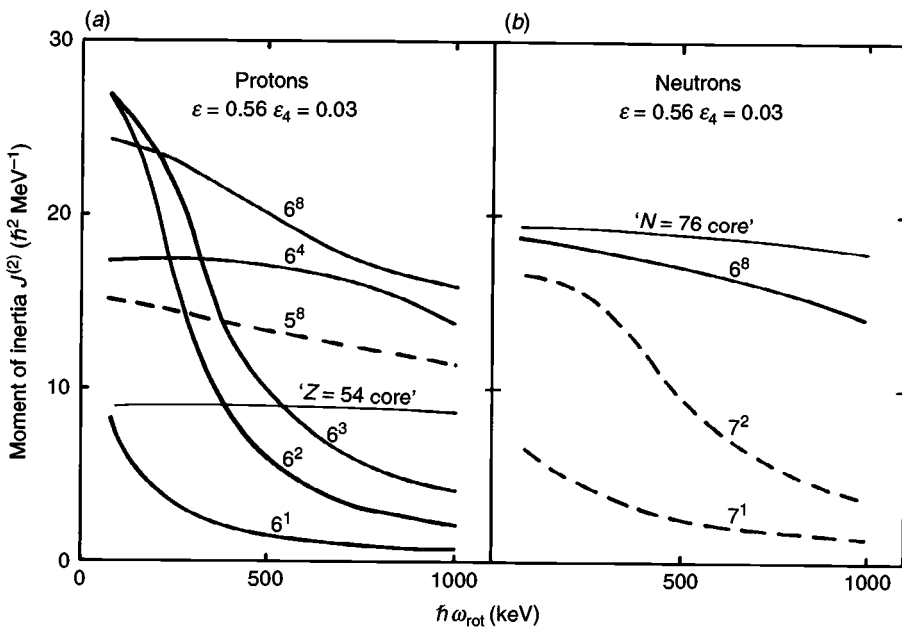


Fig. 12.21. At a deformation, typical for superdeformation in the  $A = 150$  region, the contribution to the  $\mathcal{J}^{(2)}$  moment of inertia from a) protons and b) neutrons in high- $j$  shells is plotted versus the rotational frequency. The contribution from  $n$  particles in an  $N$ -shell is denoted as  $N^n$ . The lower orbitals in the  $N = 6$  shell belong to  $i_{13/2}$  and those in  $N = 7$  to  $j_{15/2}$  but as the  $j$ -shells are appreciably mixed at the large deformation, the labelling by  $N$ -shells is preferred. Furthermore, the contributions from a  $(Z, N) = (54, 76)$  core are shown. Note that this core contribution is essentially constant while large fluctuations are seen in the high- $j$  part (from Bengtsson *et al.*, 1988).

the  $\mathcal{J}^{(2)}$  moments of inertia are identical, i.e. when the spins are plotted versus transition energies (fig. 12.23), the slopes are identical. Near-identical superdeformed rotational bands have been found both in the Dy/Gd region and in the Hg/Pb region (see Janssens and Khoo, 1991, for a review). Furthermore, it has been noticed recently (Baktash *et al.*, 1992) that normal deformed rotational bands also have  $\mathcal{J}^{(2)}$  values, which are surprisingly similar in many cases.

The surprisingly large number of identical bands might suggest that some ‘new symmetry’ is involved but no such symmetry is known at present. Indeed, we are far from a more general understanding of the identical bands. Even so, it seems appropriate to discuss some of the specific features and how they can be described in simple models. We will concentrate on the Dy/Gd region where the number of identical bands is rather small (at

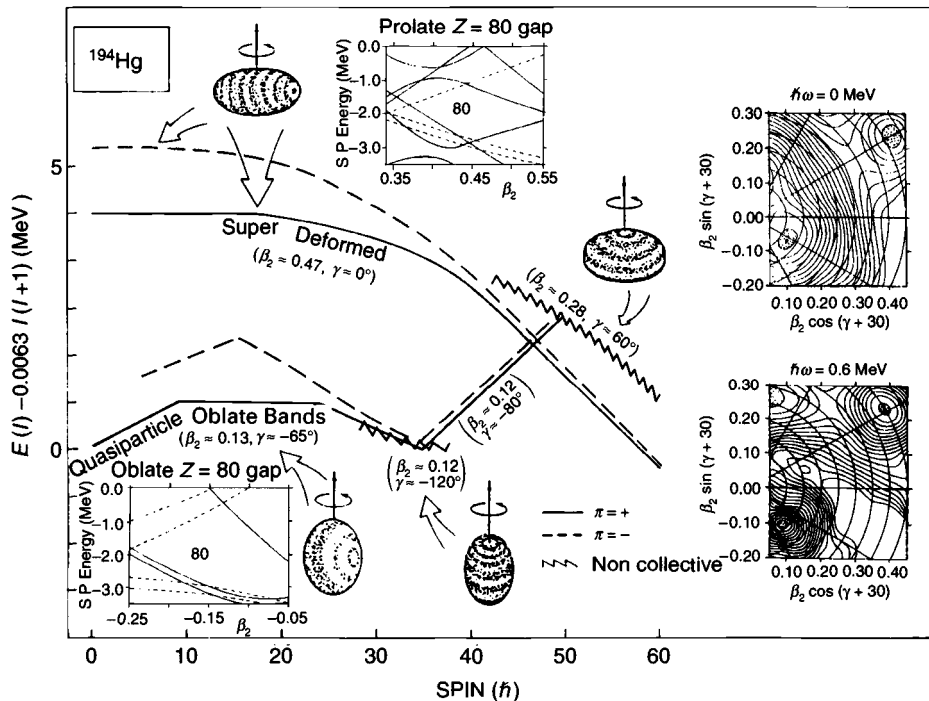


Fig. 12.22. Calculated excitation energy versus spin for  $^{194}\text{Hg}$  illustrating a rich spectrum of collective and non-collective rotations, which evolve and co-exist near the yrast line. One insert shows the shell gap at oblate shape, which stabilises an oblate ground state configuration that terminates at prolate shape ( $\gamma = -120^\circ$ ) for spins just above  $I = 30$ . Another insert shows the  $Z = 80$  gap at large prolate deformation, which is mainly responsible for the superdeformed configuration. Energy surfaces to the right indicate the corresponding minima at no rotation and at a high rotational frequency (M.A. Riley *et al.*, *Nucl. Phys.*, 1990, **A512**, 178).

present) but those cases that have been observed are very distinct, extending over a large range of frequencies. This is illustrated in fig. 12.23 where the transition energies of  $^{152}\text{Dy}$  are compared with those of superdeformed bands in neighbouring nuclei. The figure is drawn assuming specific values for the spins. If all the bands were shifted up or down by the same value in spin, this would change nothing in our conclusions. However, the relative spin assignments are crucial and although very reasonable, we must remember that they have not been measured.

The excitation energy versus spin,  $E(I)$ , for the superdeformed bands can (at least locally) be approximated by the parabola

$$E(I) \approx E_0 + AI(I + 1)$$

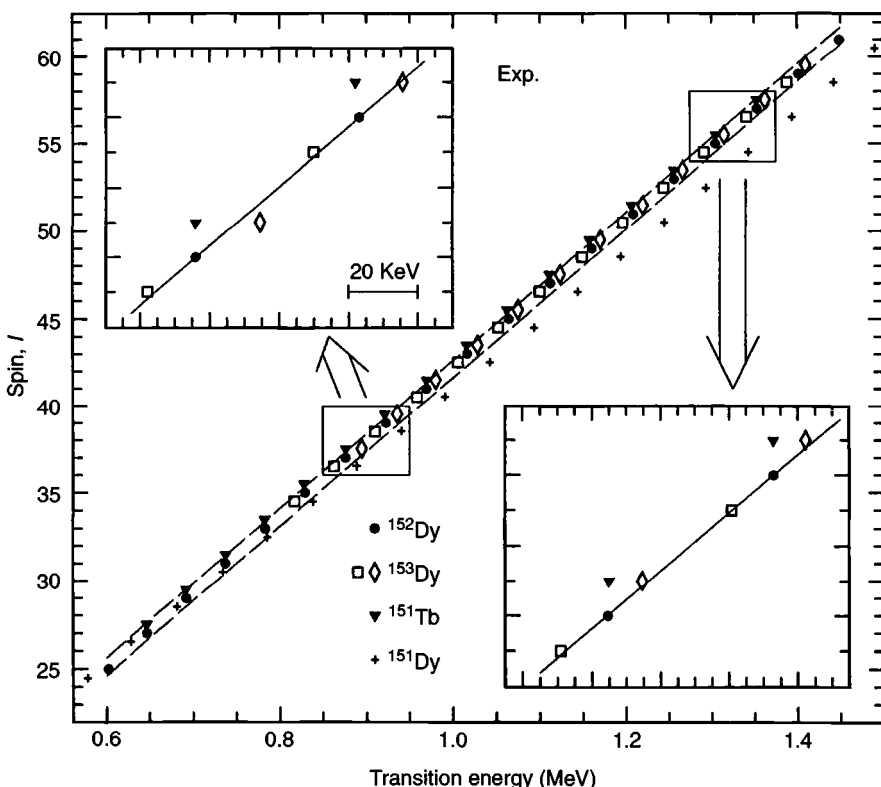


Fig. 12.23. Observed transition energies at superdeformation for  $^{152}\text{Dy}$ , two bands in  $^{153}\text{Dy}$  and the second band in  $^{151}\text{Tb}$ . The bands are drawn as spin  $I$  versus transition energy  $E_\gamma$ . The functional dependence is very close to linear as indicated by straight dashed lines. In the insets, different parts are magnified with straight lines through the  $^{152}\text{Dy}$  points. One finds that, within about 1–2 keV, the  $^{152}\text{Dy}$  and  $^{153}\text{Dy}$  data points (except one transition in  $^{153}\text{Dy}$ ) follow the same curve while the  $^{151}\text{Tb}$  and  $^{152}\text{Dy}$  data points have identical  $E_\gamma$  values. In the main figure, the  $^{151}\text{Dy}$  data points are also included to show 'large' differences between superdeformed bands.

to a high accuracy. This means that the relation between the spin  $I$  and the quadrupole transition energies,  $E_\gamma$ , is approximately linear, namely

$$E_\gamma(I) = E(I + 1) - E(I - 1) \approx A(4I + 2)$$

as comes out in fig. 12.23. Consequently, the energy difference between two consecutive transitions is roughly constant

$$\Delta E_\gamma(I) = E_\gamma(I + 1) - E_\gamma(I - 1) \approx 8A$$

Consider now the case that the excitation energy,  $E(I) - E(I = 0)$ , is described by the same function for a rotational band in an even and an

odd nucleus. Then, when plotted as in fig. 12.23, all transitions will lie on the same line but because the spins are half-integer in the odd nucleus and integer in the even, the points of the two bands will be displaced relative to each other. Thus, with the even nucleus band as reference, the points in the odd nucleus will be displaced upwards or downwards by  $\Delta E_\gamma/4$  depending on whether the spins in the odd nucleus are  $0.5\hbar$  larger or smaller than the spins in the even nucleus.

It turns out that two bands in  $^{153}\text{Dy}$  are identical to the yrast superdeformed band in  $^{152}\text{Dy}$  in the way described here, i.e. that both the upward and the downward shift are realised. In fact, such bands come out from the most simple realisation of strong coupling discussed in chapter 11. In a simplified cranking model, assuming constant deformation and no pairing, such bands result if the orbital of the odd particle shows no alignment. This is easily seen if, starting from the cranking Hamiltonian, the expectation value with respect to the single-particle state  $|i\rangle$  is taken:

$$e_i = e_i^\omega + \hbar\omega\langle j_x \rangle_i$$

With  $\langle j_x \rangle_i = 0$ ,  $e_i = e_i^\omega = \text{constant}$ , the total energy  $E_{\text{sp}}$  is changed by a constant while the total spin  $I$  remains unchanged (cf. fig. 12.24). When comparing two nuclei, an additional factor is that  $\hbar\omega_p$  and  $\hbar\omega_n$  depend on the number of protons and neutrons (chapter 8). This is, however, a small correction, see below.

For an orbital with  $\langle j_x \rangle = 0$  independently of rotational frequency  $\omega$ , the two branches with different signature will be degenerate but depending on in which of these orbitals the odd particle is put, the spin values realised are increased (signature  $\alpha = 1/2$ ) or decreased (signature  $\alpha = -1/2$ ) by  $0.5\hbar$ . Examples of orbitals that approximately fulfil the requirement of  $\langle j_x \rangle = 0$  in fig. 12.16 are [303 7/2] in the  $Z = 40$  region or [413 5/2], which is the 67th orbital at  $\omega = 0$ . For neutron particle states above ' $N = 86$ ', the [402 5/2] orbital (cf. fig. 8.3) is of similar nature and could thus be responsible for the two bands in  $^{153}\text{Dy}$ .

Even in more complete cranking calculations including shape polarisation, e.g. using the harmonic oscillator or the modified oscillator potential (see e.g. Ragnarsson, 1990; Szymański, 1990), it turns out to be rather easy to get out near-identical bands in calculations. Let us illustrate this by considering the rotating oscillator model in some detail. Thus, fig. 12.24 presents a comparison between calculated rotational bands in a ‘core nucleus’ ( $^{152}\text{Dy}$ ) and ‘core plus valence particle nucleus’ ( $^{153}\text{Dy}$ ), where the valence particle is placed in different orbitals. The differences between the calculated bands are illustrated as the difference between the  $I$  versus  $E_\gamma$  curves (of the type drawn

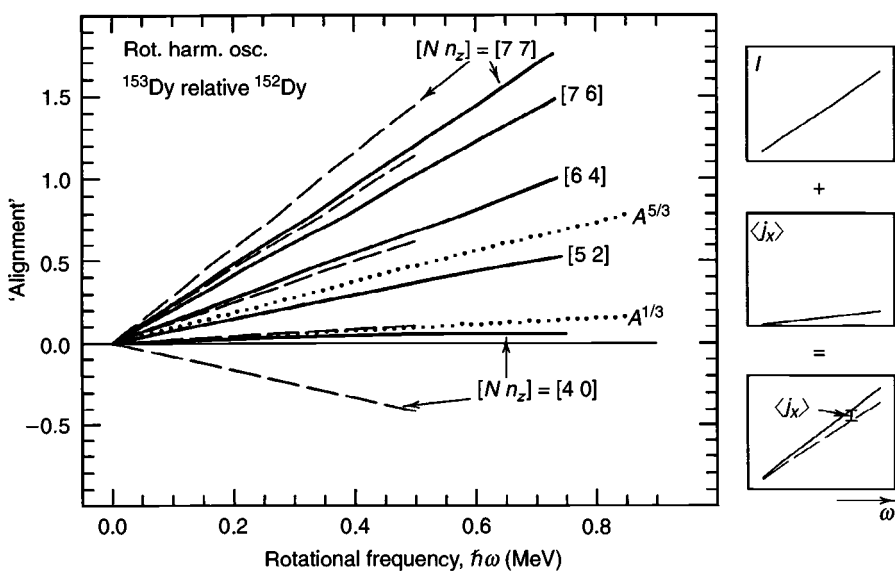


Fig. 12.24. Changes in transition energies ( $E_\gamma = 2\hbar\omega$ ) caused by the addition of one particle to a core nucleus as calculated in the rotating harmonic oscillator. The core is defined from the asymptotic orbitals, which are filled in the superdeformed band of  $^{152}\text{Dy}$  according to current theories. Its deformation is  $\varepsilon = 0.57$ . In the figures to the right is indicated schematically that, if a particle with alignment  $\langle j_x \rangle$  is added to a core at constant deformation, this alignment (effective) is obtained from the differences in the  $I$  versus  $\omega$  curves for the two bands. Thus,  $\langle j_x \rangle$  as calculated from the simple expression given in section 12.2 is drawn by dashed lines for the orbitals considered (assumed to have  $n_x = n_y$ ). Then we also give the calculated differences in transition energies (expressed as an effective alignment) between the core and the 'core plus particle' in a complete solution of the rotating oscillator. The important factors, in addition to the single-particle alignment, are the individual shape minimisation and the addition of an  $A^{1/3}$  factor (see dotted line) because of the  $A^{1/3}$ -dependence of  $\hbar\omega_n$ . Note that the shape minimisation tends to 'decrease the scattering' between the different orbitals and that the average effect of all orbitals comes close to an  $A^{5/3}$ -dependence.

in fig. 12.23), i.e. as a relative alignment between the different bands. It is immediately obvious that, considered as functions of rotational frequency  $\omega$ , all differences are essentially linear. Furthermore, with the valence particle in an equatorial orbital ( $n_z = 0$ ), essentially identical bands are created while the bands in the two nuclei become increasingly different with increasing  $n_z$  of the valence orbitals.

In our simplified treatment of rotating oscillator (section 12.2),  $\langle j_x \rangle \approx \text{constant} \cdot \omega$ . This relation and the relation  $I = \mathcal{J} \cdot \omega$  for the core are illustrated to the right in fig. 12.24 and it is then also shown how they add. Thus, in this approximation assuming constant deformation, the difference between

the rotational bands is simply the alignment of the particle. Consequently, the alignments for the different orbitals are drawn in fig. 12.24. Then, in a complete treatment of the rotating oscillator there are additional effects. First, the oscillator constant  $\hbar\omega_n$  varies with  $A^{1/3}$  (and a  $(N - Z)/A$  dependence, which is compensated by the sign change in the  $(N - Z)/A$  dependence of  $\hbar\omega_p$ ). This adds the same constant factor for all orbitals as illustrated in the figure. Second, the shape polarisation will change the moment of inertia of the core. Both of these corrections can be expressed as an effective alignment. The curves in fig. 12.24 are obtained from numerical calculation in the full rotating oscillator taking differences between calculated transition energies. It turns out, however, that the result would be almost the same if the different single-particle alignments curves were corrected by the change in rigid moment of inertia,  $J_{\text{rig}}(\text{core}) - J_{\text{rig}}(\text{core+particle})$  due to the  $\omega = 0$  shape change and by the  $A^{1/3}$  factor. Thus, the main features of fig. 12.24 are easy to calculate analytically using the equilibrium deformations given in section 12.2.

One could also note from fig. 12.24 that, if a mean value of all orbitals is taken observing that there are more equatorial orbitals than polar orbitals, the result will be an approximate  $A^{5/3}$ -dependence as expected for a rigid moment of inertia. In more realistic nuclear potentials, the properties of the equatorial orbitals are about the same as in the pure oscillator. As these are the most common type of orbitals, one would expect a large number of identical bands at superdeformation from this point of view. On the other hand, one might question whether the approximation of pure single-particle motion in a mean field is realistic or not.

Coming back to fig. 12.23, if we accept the ‘explanation’ given above for the bands of  $^{153}\text{Dy}$  that are identical to the band in  $^{152}\text{Dy}$ , the other identity between the  $^{152}\text{Dy}$  band and one band in  $^{151}\text{Tb}$  is straightforward to explain although it appears even more strange at first sight. The fact is that, in this case, a rotational band in an even nucleus and a band in an odd nucleus have transition energies that are indeed *identical*, i.e. not displaced due to the different quantisation of the spin values. Within the scheme we have described, this is understood as caused by an orbital that shows an alignment already at no rotation, i.e. an  $\Omega = 1/2$  orbital with a decoupling factor  $a \neq 0$  (cf. section 11.2). For an equatorial orbital of this kind, the frequency-dependence of the alignment is essentially independent of the initial alignment. Thus, we can use the same arguments as above if we only add a constant factor corresponding to the  $\omega = 0$  alignment. The identical transition energies in the bands in  $^{152}\text{Dy}$  and  $^{151}\text{Tb}$  then require an initial alignment of  $\langle j_x \rangle = -0.5$  (corresponding to  $|a| = 1$ ) for the active

orbital (the minus sign results because the particle is taken away, i.e. a hole excitation, when going from  $^{152}\text{Dy}$  to  $^{151}\text{Tb}$ ). Indeed, in the single-particle diagram, the orbital [301 1/2] has essentially the desired properties even though the decoupling factor comes out somewhat smaller than  $a = 1$  in most calculations using different potentials.

It was the observation (Byrski *et al.*, 1990) of the identical bands in  $^{152}\text{Dy}$  and  $^{151}\text{Tb}$  (and a similar identity between the yrast band in  $^{151}\text{Tb}$  and one excited band in  $^{150}\text{Gd}$ ) that really focused attention on such bands (see e.g. Stephens *et al.*, 1990) and started a lot of theoretical investigations. This was so even though the identical bands in  $^{152}\text{Dy}$  and  $^{153}\text{Dy}$  were already known, as were also two identical superdeformed bands in the  $A = 190$  region, the latter, however, over a range of fewer transitions. In the best cases, the identity of the transition energies is good within 1–2 keV extending over about 15 transitions with energies about 600–1600 keV. These numbers might, however, give the impression that the identity is even more strange than it really is. We must remember that all the superdeformed bands are very regular and follow essentially the same curve in an  $I$  versus  $E_\gamma$  diagram. This is illustrated in fig. 12.23 where we also give the transition energies for  $^{151}\text{Dy}$ . The superdeformed band in  $^{151}\text{Dy}$  is understood as being formed when one  $N = 7$  neutron is removed from  $^{152}\text{Dy}$ . Considering that these bands are found in neighbour nuclei, they are unusually different. This indicates that, if a more inert orbital is either empty or filled in two bands in neighbouring nuclei, the bands by necessity have to be rather similar. Even so, the extreme identity observed appears very strange. Furthermore, in view of the accuracy obtained in nuclear calculations in general, it is indeed surprising that the simple theories discussed here seem to describe the experimental situation so well. One would expect that different correlations not accounted for, especially pairing, would make the very detailed comparison between theory and experiment impossible. The models introduced here seem to be useful mainly in the Dy/Gd region. The superdeformed bands in the Hg/Pb region could not really be described within this scheme assuming pure single-particle degrees of freedom with no pairing. Different ideas on how the identical bands in Hg/Pb nuclei could be understood have been published e.g. by Stephens *et al.* (1990) and Azaiez *et al.* (1991). There is however no established understanding of these bands, see e.g. Baktash *et al.* (1993).

If the mechanisms for creating identical bands discussed here are qualitatively correct, it should also be possible to describe differences between bands that are not identical. One might say that to invent a theory which gives identical bands, or even bands that differ by some smooth quantity, is not

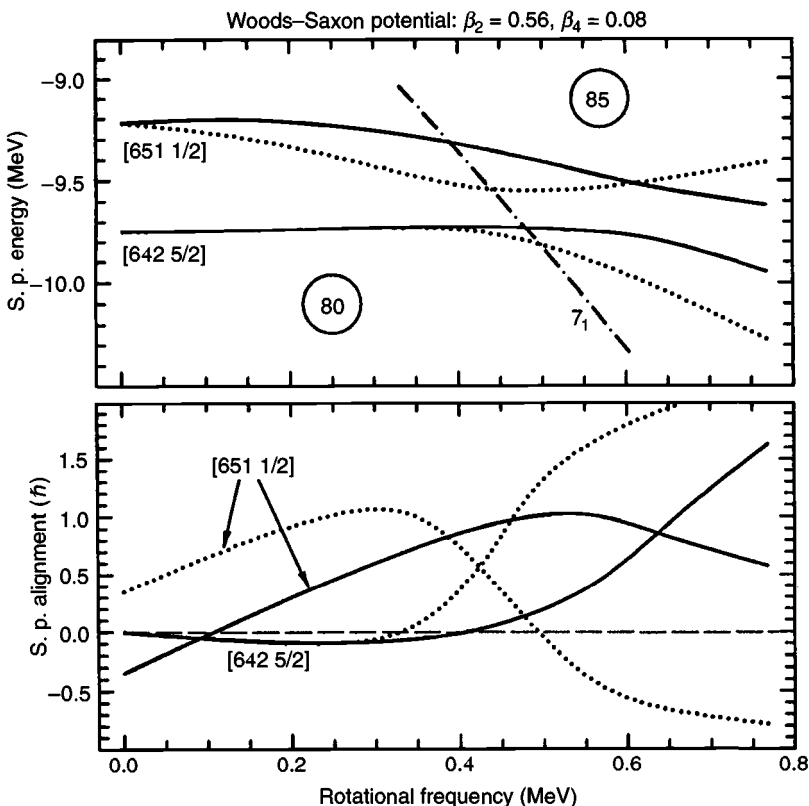


Fig. 12.25. The orbitals calculated in the Woods-Saxon potential at superdeformation in the  $N = 80$ -85 region are drawn versus rotational frequency  $\omega$  in the upper figure while the alignments of the orbitals labelled by asymptotic quantum numbers [651 1/2] and [642 5/2] are shown in the lower figure.

so difficult. A better test of some theory is its ability to describe non-smooth differences between the observed quantities. Then, the superdeformed bands observed in  $^{146-149}\text{Gd}$  are especially favourable because some of these bands show a band-crossing while others do not.

When searching for orbitals at 2 : 1 deformations and neutron numbers  $N = 82$ -85, which could give rise to an observable crossing, the only reasonable candidates seem to be the  $N = 6$  orbitals [642 5/2] and [651 1/2]. As should be evident from fig. 8.3, drawn for somewhat smaller deformations, these orbitals come close together for  $\epsilon = 0.5$ -0.55. Other crossings occur between orbitals from different  $N$ -shells and appear to interact much less than observed in experimental bands. The details of this single-particle crossing are illustrated in fig. 12.25, as calculated in the Woods-Saxon

model. The single-particle orbitals are drawn in the upper figure where a very small energy interval is considered so that only the two signature branches of these two orbitals together with the lowest  $N = 7$  orbital are seen (cf. fig. 12.16, which shows a much larger energy interval but where the crossings are drawn somewhat schematically. Consider e.g. the crossing between the [532 5/2] and [541 1/2] orbitals around  $Z = 60$  in fig. 12.16 which in many ways is similar to the crossing in fig. 12.25). In the lower part of fig. 12.25, the alignments  $\langle j_x \rangle$  of the orbitals are drawn. These alignments are proportional to the slopes in the upper figure.

In a way analogous to the identical bands, we now consider (Haas *et al.*, 1993) the differences between the transition energies of two bands in neighbouring nuclei with one orbital either filled or empty. For the orbitals of fig. 12.25, the calculated differences are drawn in the lower part of fig. 12.26. It is evident that this figure has the same structure as the alignments in fig. 12.25 and it is straightforward to see which orbital is either empty or filled when comparing two bands. The differences when comparing the two figures arise mainly from the fact that the Woods-Saxon potential has been used in one figure and the modified oscillator in the other. Furthermore, in fig. 12.26, we compare rotational bands which have been minimised in deformation independently while in fig. 12.25, the single-particle alignment  $\langle j_x \rangle$  is shown. The comparison shows that, in the present formalism corresponding to single-particle motion in a mean field, it is the alignment of the specific orbitals which is the important factor and that e.g. deformation changes between different bands will only lead to minor corrections.

In the upper panel of fig. 12.26, the differences in transition energies between the observed bands are drawn. The large similarity between experiment and theory in fig. 12.26 seems to be very strong evidence that our interpretation of which orbitals are active is really correct. In drawing the experimental figure, one has to make specific assumptions about the relative spins but now it seems possible to turn the argument around, claiming that the good agreement between theory and experiment means that we have determined these relative spins. This would mean that, if it becomes possible to measure the spin values in one superdeformed band, we might extract the spins also for the bands in neighbouring nuclei. Indeed, in a recent paper (Atac *et al.*, 1993), it has been claimed that the spins in the superdeformed band of  $^{143}\text{Eu}$  have been measured. At present, very few superdeformed bands are known in neighbouring nuclei of  $^{143}\text{Eu}$  so it does not seem possible to carry out a similar analysis around  $^{143}\text{Eu}$  as for  $^{146-149}\text{Gd}$ .

The cases we have chosen in fig. 12.26 are not really typical but more

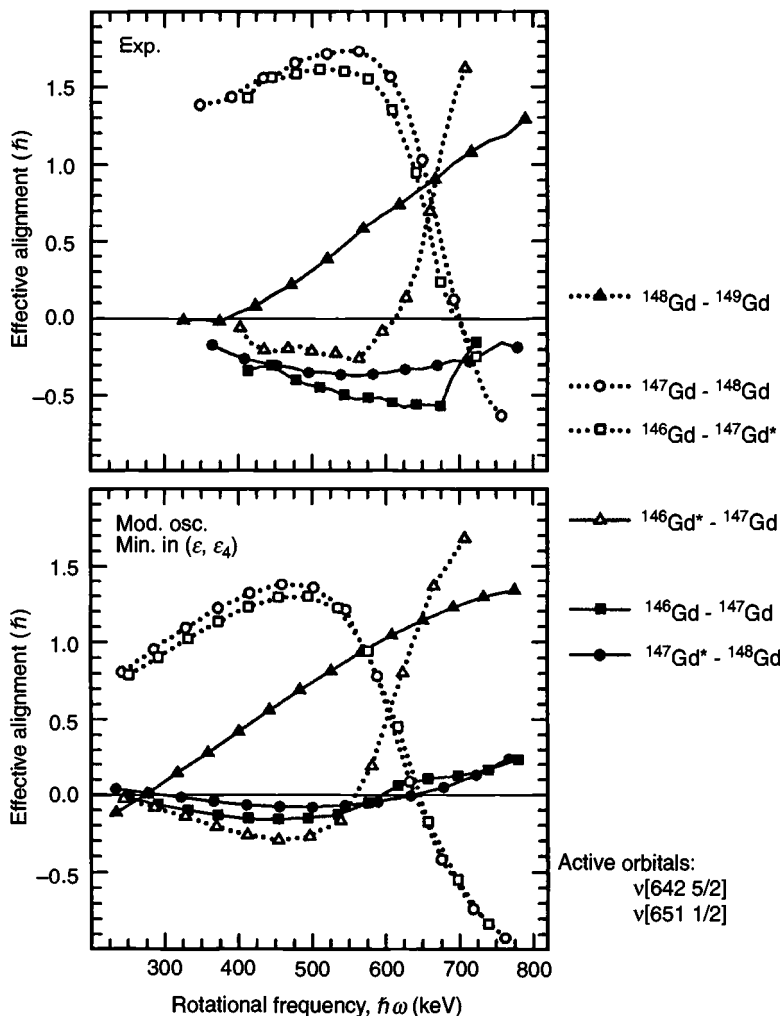


Fig. 12.26. The upper figure shows the relative transition energies for superdeformed bands in  $^{146-149}\text{Gd}$  where an asterisk indicates the ‘second’ band in that nucleus. The differences are plotted as (effective) alignments extracted as indicated in the lower right panel of fig. 12.24 ( $\omega = E_\gamma/2$ ). Effective alignments extracted in the same way from rotational bands calculated in the modified oscillator are shown in the lower figure. A comparison with fig. 12.25 shows that it is the orbital that is labelled by  $[651\ 1/2]$  at  $\omega = 0$  and has  $\langle j_x \rangle > 0$  (the signature  $\alpha = -1/2$  branch), which is being filled in the calculations when going from  $^{147}\text{Gd}$  to  $^{148}\text{Gd}$  or from  $^{146}\text{Gd}$  to  $^{147}\text{Gd}^*$  etc. A comparison between the upper and lower figure strongly suggests a one to one correspondence between those orbitals used in the calculations and those active in the observed bands.

specific cases where theory and experiment seem consistent almost to the fine details. Even so, the comparison suggests that the superdeformed bands are really the best chance to see pure single-particle effects in nuclei. In the future, we could hope that a large number of rotational bands will be observed at different deformations (where favoured proton and neutron shell effects are ‘in phase’). Thus, it might be possible to map the single-particle orbitals all the way from the ground state to two separated fragments. In this sense, nuclei are a very special laboratory in our study of quantum many-body physics.

Some more details of the cranking calculations have been reviewed in a recent paper (Bengtsson *et al.*, 1991) where also computer codes on a floppy disc are provided. The theoretical model behind the calculated energies shown in fig. 12.22 is somewhat different from the simple cranking model presented here. Specifically, the pairing interaction (chapter 14) is included. This should make the calculations more realistic in most cases but it has the disadvantage that they become less transparent and it becomes difficult to plot energy surfaces as functions of the physical quantity  $I$  or to follow the evolution of fixed configurations. Thus, the energy surfaces shown in fig. 12.22 are a mixture of different configurations (similar to fig. 12.8 for  $^{160}\text{Yb}$ ) and as they are drawn for a fixed rotational frequency, the spin  $I$  might be different at different deformations. Attempts to overcome these deficiencies have been made recently (Bengtsson, 1989). One could also note that, even within the simplified model described here, all the structures of fig. 12.22 come out (see calculations on  $^{187}\text{Au}$  by Bengtsson and Ragnarsson, 1985) although in a somewhat qualitative way for low spins.

The recent discoveries of the superdeformed bands have thus made it possible to test theoretical predictions of the single-particle structure and the shell effects at large deformation. Fig. 12.15 suggests that favoured shell effects are present at large deformations for essentially all particle numbers. Thus, we would expect that, correlated with the particle number, rotational bands will be identified for essentially all deformations up to very elongated shapes, e.g. at 3 : 1 axis ratio. In this way it should be possible to scan large parts of fig. 12.15 and test how well the predictions are realised. One can then also start to ask more detailed questions about how large deformations and/or rotation disturb the nuclear quantal system.

### Exercises

- 12.1 A particle of mass  $m$  is subject to the laws of classical mechanics. The motion of the particle can be described either in a laboratory

system,  $x$ ,  $y$  and  $z$  or in another system  $x_1$ ,  $x_2$  and  $x_3$ , which rotates with a constant angular frequency,  $\omega$ , around the  $x$ -axis (equal to the  $x_1$ -axis). The potential energy only depends on the coordinates in the rotating system,  $V = V(x_1, x_2, x_3)$ . Find the Hamiltonian in the rotating system and compare with the cranking Hamiltonian.

- 12.2 The nuclear single-particle potential is built from the mutual interaction of the individual nucleons. Therefore, it is important that the shape built from the nuclear density distribution is similar to the potential shape. In a non-rotating harmonic oscillator, this is easily verified. Thus, one finds that, if the energy of an arbitrary configuration is minimised with respect to deformation, the ratio of expectation values,  $\langle x_1^2 \rangle : \langle x_2^2 \rangle : \langle x_3^2 \rangle$  is the same for the density distribution as for the potential. Show this!
- 12.3 In the discussion of the rotating oscillator model, the self-consistent frequencies were derived as  $\omega_i = \omega_0^0 \left( \Sigma_1 \tilde{\Sigma}_2 \tilde{\Sigma}_3 \right)^{1/3} / \tilde{\Sigma}_i$ . Use this expression together with the definitions of the quadrupole deformation parameters,  $\varepsilon$  and  $\gamma$ , to calculate how these latter parameters vary with spin,  $I$ .
- 12.4 Derive the static moment of inertia

$$\mathcal{J}_{\text{stat}} = M \sum_{v_{\text{occ}}} \left\langle v \left| y^2 + z^2 \right| v \right\rangle$$

- for independent particles in a rotating harmonic oscillator potential.  
12.5 In the harmonic oscillator model, the ground state energy is given as

$$E = 3\hbar\omega_0^0 (\Sigma_x \Sigma_y \Sigma_z)^{1/3}$$

as derived in the main text. Use this formula to determine the distribution of quanta in the ground state of  $^{24}\text{Mg}$ . Then, apply the simplified formulae for the cranked harmonic oscillator to calculate  $E(I)$ ,  $\varepsilon(I)$  and  $\gamma(I)$  for the three bands that result from rotation around the three principal axes.

- 12.6 Calculate the rotational frequency for rigid rotation of a spherical  $^{20}\text{Ne}$  nucleus at angular momentum  $I = 8$ . Which angular momentum will result for a spherical  $A = 160$  nucleus that compared with  $^{20}\text{Ne}$  has
- (a) the same rotational frequency;
  - (b) the same velocity at the nuclear surface?